Quantum Transport in Graphene Heterostructures

A Thesis

submitted to
Indian Institute of Science Education and Research Pune in partial fulfillment of the requirements for the BS-MS Dual Degree Programme
by

Debarghya Basak

Indian Institute of Science Education and Research Pune
Dr. Homi Bhabha Road,
Pashan, Pune 411008, India.

April, 2025
Supervisor: Prof. Hryhoriy Polshyn
Debarghya Basak

Certificate

This is to certify that this dissertation entitled Quantum Transport in Graphene Heterostructures towards the partial fulfillment of the BS-MS dual degree Programme at the Indian Institute of Science Education and Research, Pune represents study/work carried out by Debarghya Basak at the Institute of Science and Technology under the supervision of Hryhoriy Polshyn, Assistant Professor, during the academic year 2024-2025.

Prof. Atikur Rahman

Hryhoriy Polshyn

Prof. Hryhoriy Polshyn

Committee:

Prof. Hryhoriy Polshyn (ISTA)

Prof. Atikur Rahman (IISER Pune)

Declaration

I hereby declare that the matter embodied in the report entitled 'Quantum Transport in Graphene Heterstructures' are the results of the work carried out by me at the Institute of Science and Technology (ISTA) Austria, under the supervision of Prof. Hryhoriy Polshyn, and the same has not been submitted elsewhere for any other degree. Wherever others contribute, every effort is made to indicate this clearly, with due reference to literature and acknowledgement of collaborative research and discussions.

Debarghya Basak

Roll Number: 20201097

Abstract

This thesis investigates quantum transport phenomena in graphene heterostructures, focusing specifically on twisted monolayer-bilayer graphene (tMBG). Graphene, known for its exceptional electrical properties, exhibits unique behaviours when arranged in twisted configurations, giving rise to moiré superlattices. These structures dramatically alter graphene's electronic band structure, enabling the study of emergent quantum phenomena such as correlated insulating states, quantum anomalous Hall effect and superconductivity.

We report detailed studies on the fabrication of high-quality tMBG devices and its characterization. Mechanical exfoliation and dry-transfer methods were optimized to produce clean and uniform graphene layers, which were precisely twisted to specific angles. To ensure accurate control of the heterostructure assembly, we used advanced methods like Atomic Force Microscope (AFM) lithography, facilitating precise patterning and modification of graphene layers.

Transport measurements conducted at low temperatures (1.5 K) revealed distinct insulating phases at specific carrier densities, corresponding to the existence of flat electronic bands. Notably, we observed insulating states at complete and partial fillings of the moiré superlattice bands, highlighting strong electron-electron interactions. Furthermore, van Hove singularities were identified and shown to be tunable by the applied displacement field.

Additionally, we explored Lateral Force Microscopy (LFM) as a technique for imaging moiré patterns in twisted graphene structures at ambient conditions. Through careful analysis, periodicities consistent with the expected moiré superlattice dimensions were successfully identified, demonstrating the technique's potential for characterizing local twist-angle disorder.

Finally, a quantum point contact (QPC) device using Bernal-stacked bilayer graphene was fabricated, showcasing robustness under high DC bias and setting a foundation for future explorations into quantized conductance channels.

This work underscores the rich and tunable physics accessible in graphene heterostructures, providing pathways for further research into quantum electronics and novel device architectures.

Contents

List of Figures

List of Tables

Acknowledgements

At the outset, I extend my sincere gratitude to Prof. Hryhoriy Polshyn, for his guidance, support, and motivation throughout this work. The experience of working under his supervision has greatly shaped my understanding of scientific research. His unwavering optimism in every situation has instilled in me the resilience to tackle challenging problems. His insights during group meetings and expertise in troubleshooting problems have played a crucial role in shaping this work.

I would like to thank Prof. Atikur Rahman, for agreeing to be a part of my thesis committee and for all the valuable advice that helped improve the quality of this thesis.

I want to thank my fellow group member, Maosen Qin for his limitless patience for my questions and engaging discussions that taught me more than I could learn from articles alone. His infectious work ethic and his willingness to help me process my devices made this thesis possible.

I would like to show my gratitute towards my friends Sachin, Gaurang, Ritesh, and Dhruv for the countless discussions and debates we had throughout our undergraduate years.

I am profoundly thankful to my parents for their encouragement and belief in me. Their unwavering support has been the cornerstone of my academic journey.

Lastly, I want to acknowledge the two places that shaped my academic experience. Pune, with its youthful energy and vibrant atmosphere, provided the perfect backdrop for the challenging yet fulfilling pursuit of a degree in physics. In contrast, Maria Gugging, nestled in the serene suburbs of Vienna, offered a peaceful and picturesque setting. The sense of calm I found there made working on my thesis all the more enjoyable.

This thesis is dedicated to my parents.

Chapter 1

Introduction

1.1 Overview

Graphene is a planar arrangement of carbon atoms that form a honeycombs lattice. It was long theorized to exist, but too unstable to be isolated in free form. The breakthrough happened in 2004 when Andre Geim and Konstantin Novoselov at the University of Manchester managed to isolate graphene[28] by using 'Scotch Tape' to isolate thin layers from a graphite crystal. This method of mechanically exfoliating graphene made it possible to study its properties in the laboratory setting. This technique was soon applied to other layered van der Waals materials which resulted in birth of the rapidly advancing field of engineered 2D materials.

In this study, we will look at the heterostructures of graphene. As an atomically flat substrate, we use hexagonal Boron Nitride (hBN). The use of hBN as a substrate for graphene devices was first demonstrated[10] by the groups of Philip Kim and James Hone at Columbia

University. Owing to matching lattice dimensions of graphene and hBN, these materials can be stacked without inducing any strain or defects in graphene, so that there are no changes to the inherent properties of graphene[1]. The big band-gap (5.97 eV) and, the dielectric properties of hBN ($\epsilon \approx 3-4$ and $V_{breakdown} = 0.7$ V nm^{-1})[1], make it a comparable gate dielectric to SiO_2 used in conventional Si-based transistors.

While Van Hove singularities arising from the moiré pattern in CVD (Chemical Vapour Deposition) grown graphene layers were observed as early as 2010[22], the first deliberate twisting of two graphene layers was demonstrated by Kim et al. (2016)[20]. This technique was further refined by Pablo Jarillo-Herrero's group at MIT in 2018[6][5]. They stacked one graphene layer on top of another and twisted them at a 'magic angle' of 1.1°. This resulted in the observation of correlated insulating states[5] and superconductivity[6] in this system. This discovery started the field of 'twistronics'. Since then a lot of different twisted graphene systems have been studied. These systems exhibit a lot of interesting phenomena like superconductivity, correlated insulating states and orbital ferromagnetism.

The system that we are focused on is the twisted monolayer-bilayer system. In this system, a single layer of graphene is twisted against a layer of Bernal stacked bilayer graphene. Phenomena like the quantum anomalous Hall effect (QAHE)[32], orbital ferromagnetism and electrically tunable correlated insulating states[29][39][7][15] have been reported in this system. In this study, we will try to optimise the transfer process of twist graphene heterostructures with the aim of achieving higher quality devices with lower twist-angle disorder.

We will start by discussing the relevant theoretical background for system under study and the different phenomena that this system exhibits.

1.2 Theoretical Background

1.2.1 Graphene[14]

The lattice constants of graphene(hexagonal lattice) are written as:

$$a_1 = a\left(\frac{\sqrt{3}}{2}, \frac{1}{2}\right) \quad a_2 = a\left(\frac{\sqrt{3}}{2}, \frac{-1}{2}\right) \tag{1}$$

The lattice can be described a Bravais lattice with these lattice vectors, and the unit cell is marked by the shaded parallelogram in Fig. 1a. The unit cell therefore encloses two

inequivalent carbon atoms labelled 1 and 2.

$$b_1 = \frac{2\pi}{a}\left(\frac{1}{\sqrt{3}}, 1\right), \quad b_2 = \frac{2\pi}{a}\left(\frac{1}{\sqrt{3}}, -1\right) \tag{2}$$

Vectors b_1 and b_2 define the reciprocal lattice (also a hexagon). The first Brillouin Zone (BZ) is shown as light blue region in Fig. 1b. This region is bounded by the perpendicular bisectors of the reciprocal lattice vectors. The points enclosing the BZ are called K-points, with two inequivalent corners: K and K', given by:

$$K = \frac{2\pi}{3a}\left(1, \sqrt{3}\right), \quad K' = \frac{2\pi}{3a}\left(1, -\sqrt{3}\right) \tag{3}$$

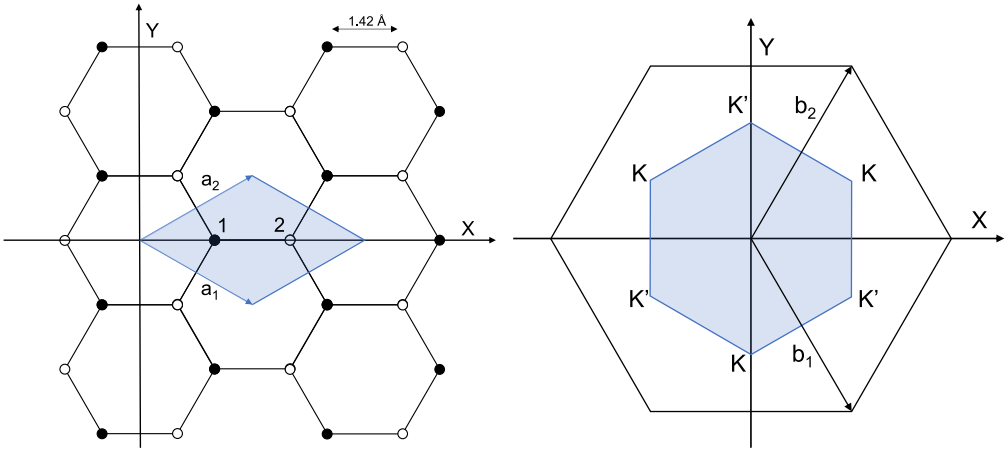

(a) Graphene Lattice (b) First Brillouin Zone

Figure 1: Description

Now, the hexagonal lattice can be broken down into triangular sub-lattices, A and B, represented as black and white circles in Fig. 1a. Graphene's dispersion relation can now, be obtained by using tight binding calculations, where only next-nearest neighbour hopping is considered for a sublattice. The Hamiltonian for this system is:

$$H = -t \sum_{\langle i,j,\sigma \rangle} a^{\dagger}_{i\sigma} b_{j\sigma} + h.c. \tag{4}$$

Here, $a^{\dagger}_{i\sigma}$ is an electron creation operator at site i for sublattice A with spin σ, and $b^{\dagger}_{j\sigma}$ is an annihilation operator at site j with spin σ on sublattice B, with t being the hopping parameter. Now, a wavefunction can be written with two components, one for each

sublattice:

$$\begin{pmatrix} \alpha_{\mathbf{k}} \\ \beta_{\mathbf{k}} \end{pmatrix} = \sum_i e^{i\mathbf{k}.\mathbf{R_i}} \begin{pmatrix} a_i^\dagger e^{-i\mathbf{k}.\boldsymbol{\Delta}/2} \\ b_i^\dagger e^{i\mathbf{k}.\boldsymbol{\Delta}/2} \end{pmatrix} \tag{5}$$

Here, Δ is the vector connecting the two sublattices (nearest neighbours), and R_i is the reference vector for the ith unit cell. The Hamiltonian then becomes:

$$H = \begin{pmatrix} 0 & f_{\mathbf{k}} \\ f_{\mathbf{k}}^* & 0 \end{pmatrix} \tag{6}$$

Where, $f(\mathbf{k}) = -t\sum_\Delta e^{-i\mathbf{k}.\boldsymbol{\Delta}}$ and Δ are the nearest neighbour vectors. Then, the energy eigenvalues can be calculated as:

$$E(\mathbf{k}) = \pm|f_{\mathbf{k}}| \tag{7}$$

$$= \pm t\sqrt{1 + 4\cos\left(\frac{\sqrt{3}a}{2}k_x\right)\cos\left(\frac{a}{2}k_x\right) + \cos^2\left(\frac{a}{2}k_y\right)} \tag{8}$$

Shown in Fig. 2 are the energy bands. The bands coincide at the K/K' points, called Dirac points. On expanding the dispersion relation around the K point by taking $\boldsymbol{\kappa} = \mathbf{k} - \mathbf{K}$, we get:

$$f_{\mathbf{K}}(\boldsymbol{\kappa}) = -\frac{3\sqrt{3}}{2a}te^{-iK_xa/\sqrt{3}}(i\boldsymbol{\kappa}_x - \boldsymbol{\kappa}_y) + O(\boldsymbol{\kappa}^2) \tag{9}$$

$$\approx \hbar v_F(\boldsymbol{\kappa}_x + i\boldsymbol{\kappa}_y) \tag{10}$$

Where the Fermi velocity of electrons in graphene is $v_F = \frac{\sqrt{3}ta}{2\hbar}$. And $f_{K'}(\boldsymbol{\kappa}) = f_K^*(\boldsymbol{\kappa})$. Therefore, the effective Hamiltonian around the Dirac point near low energies is:

$$H = \begin{pmatrix} 0 & f_{\mathbf{k}}(\boldsymbol{\kappa}) \\ f_{\mathbf{k}}^*(\boldsymbol{\kappa}) & 0 \end{pmatrix} = \hbar v_F \begin{pmatrix} 0 & \boldsymbol{\kappa}_x + i\boldsymbol{\kappa}_y \\ \boldsymbol{\kappa}_x - i\boldsymbol{\kappa}_y & 0 \end{pmatrix} = \hbar v_F \boldsymbol{\sigma}.\boldsymbol{\kappa} \tag{11}$$

And the energy eigenvalues are:

$$E(\boldsymbol{\kappa}) = \pm\hbar v_F|\boldsymbol{\kappa}| \tag{12}$$

Eq. 11, the effective Hamiltonian of graphene near small energy values, is the famous Dirac Hamiltonian for massless relativistic particles. From the energy spectrum in Fig. 2, we see that the minima of the conduction band and the maxima of the valence band coincides near the six K/K' points. Considering the single Dirac point on the second half of Fig. 2, we see the linear relationship of energy and momentum of electrons in graphene close to the

K/K' points. The electrons behave like massless Dirac fermions[1]. The spinor associated with the Hamiltonian resembles the spin degree of freedom and is thus called pesudospin. The pseudospin follows the momentum of the electron. This gives rise to the phenomena of chiral transport in graphene, where the electrons move along the direction of their pseudospin.

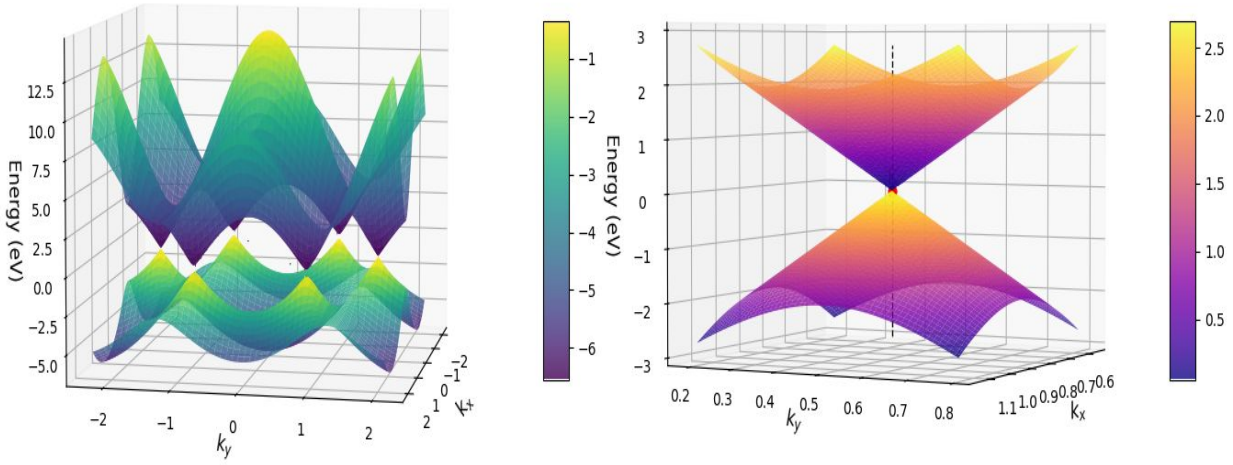

Figure 2: Left panel: Dispersion Relation of graphene. Right panel: Zoomed in view of the band structure near one Dirac points

1.2.2 Quantum Hall Effect[35]

When a 2D electron gas is subject to a magnetic field (B), we can observe some quantized energy levels. The energy levels are quantized into Landau levels, which are equally spaced in energy. We can approach this semi-classically by considering the behaviour of the electrons in a magnetic field:

$$H = \frac{1}{2m}\left(\mathbf{p} + \frac{e}{c}\mathbf{A}\right)^2 \tag{13}$$

Where, $\mathbf{A}$ is the vector potential[11]. The electrons are bound to the x-y plane, while the constant magnetic field is considered to out of plane, such that $\nabla \times \mathbf{A} = B\hat{\mathbf{z}}$. We can write the canonical momentum as, $\boldsymbol{\pi} = m\mathbf{p} + e\mathbf{A}$. The Hamiltonian is as follows:

$$H = \frac{1}{2m}\boldsymbol{\pi}\cdot\boldsymbol{\pi} = \hbar\omega_B\left(a^\dagger a + \frac{1}{2}\right) \tag{14}$$

Where, $\omega_B = \frac{eB}{mc}$ is the cyclotron frequency, and $a = \frac{1}{\sqrt{2e\hbar B}}(\pi_x - i\pi_y)$ is the raising operator and $a^\dagger = \frac{1}{\sqrt{2e\hbar B}}(\pi_x + i\pi_y)$ is the lowering operator. Similar to the harmonic oscillator, the energy eigenvalues are:

$$E_n = \hbar\omega_B\left(n + \frac{1}{2}\right) \quad n \in \mathbb{N} \tag{15}$$

These energy levels are the Landau levels. A crucial difference from the energy levels of the harmonic oscillator is large degeneracy of the Landau levels. Landau levels have the following degeneracy[11]: $g = \frac{eB}{hc}A$, where A is defined as the area of the 2D plane.

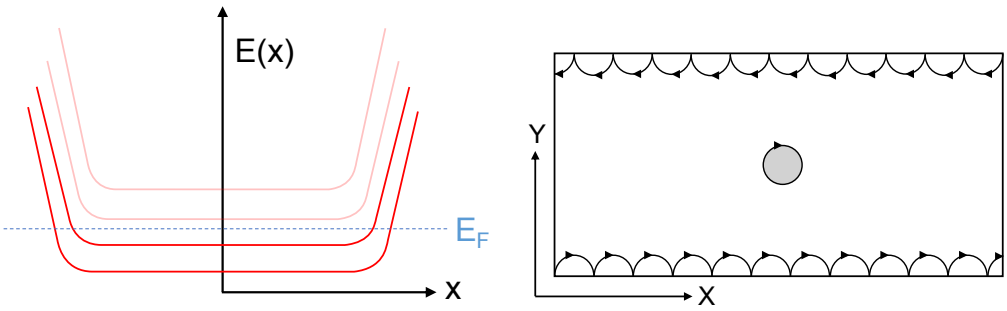

(a) Landau Levels at the edge (b) Edge modes

Figure 3: Description

If we consider the cyclotron orbit of the electrons at the edge of the 2D plane, we see that the electrons collide with the boundary. But as they are bound to orbit along the orbit dictated by the constant magnetic field, they skip along the boundary resulting in the formation of edge states. These edge states are shown in Fig. 3b. The edge states are chiral, meaning that they move in one direction along the edge of the 2D plane. They have opposite chirality on the opposite edges which ensures that the net current is zero without the presence of an electric field. The edge states are topologically protected, meaning that they are robust against perturbations that are time-reversal symmetric. This is because to disrupt the edge states, electrons of opposite chiralities would have to scatter off each other which is not possible due to the presence of the bulk. The edge states are responsible for the quantized Hall conductance. The Hall resistance is given by:

$$R_{xy} = \frac{V_y}{I_x} = \frac{h}{e^2}\frac{1}{\nu} = \frac{B}{ne} \tag{16}$$

Here, ν is filling factor, n is electron density, e is electronic charge. The Hall resistance is quantized in units of $\frac{h}{e^2}$. From the above expression we can find the density required to fill ν Landau levels:

$$n = \frac{B}{\Phi_0}\nu \tag{17}$$

Where, $\Phi_0 = \frac{h}{e}$ is the flux quantum. So when the filling factor is some integer $\nu = n$, we have n edge modes contributing to the transport (Fig. 3a). This means that R_{xy} is quantized to $\frac{h}{e^2}\nu$ and since the edge modes are chiral and cannot be scattered into each other, the longitudinal resistance (R_{xx}) is zero. This would explain the quantization of the Hall resistance, but the width of the Hall plateaus and their persistence over a range of magnetic fields can only be understood by the existence of disorder. In experimental samples, there is always some disorder. The disorder can be modelled as a random potential (V) in the Hamiltonian such that the disorder is much less than the energy difference of the Landau levels,

$$\frac{V}{\hbar\omega_B} \ll 1 \tag{18}$$

This means that for the observation of Quantum Hall Effect[11], the sample has to be extremely clean and the disorder has to be minimal. Now the disorder in the system results in the Landau levels broadening into Landau bands, due to the existence of localized states in the bulk of the sample. This results in the Hall resistance being quantized to $\frac{h}{e^2}\nu$ spanning a spectrum of B field, which is the hallmark of the Quantum Hall Effect.

1.2.3 Berry Phase and Chern number in Quantum Hall Effect[35]

The quantized of the Hall conductance can be understood in terms of the topological characteristics of the system. To see this, we will consider the Berry phase acquired by the wavefunction of the electrons as they move in the Brillouin Zone. We consider a system described by the Hamiltonian $H = H(\lambda)$, where λ is a parameter that varies adiabatically in time, such that there is no level crossing. The eigenstates of the Hamiltonian are $|n(\lambda)\rangle$ with eigenvalues $E_n(\lambda)$. If we now look at the evolution of the wavefunction over a path C in the parameter space, we can write the wavefunction as:

$$|\psi_n(\lambda)\rangle = e^{i\gamma_n(t)} exp\left(-\frac{i}{\hbar}\int_0^t dt' E_n(\lambda(t'))\right)|n(\lambda(t))\rangle \tag{19}$$

Where, $\gamma_n(t)$ is the Berry phase. The second exponent is the dynamical phase factor. Plugging this into the Schrödinger equation $i\hbar\frac{\partial}{\partial t}|\psi_n(t)\rangle = H(\lambda(t))|\psi_n(t)\rangle$, and multiplying by

$\langle n(\lambda(t))|$ on both sides, we can get the Berry Phase:

$$\gamma_n = \oint_C d\lambda \cdot A_n(\lambda) \tag{20}$$

Where, $A_n(\lambda) = i\langle n(\lambda)|\nabla_\lambda|n(\lambda)\rangle$ is the Berry connection. The Berry connection is analogous to the magnetic vector potential. It is defined as the curl of the Berry connection, $\Omega_n = \nabla_\lambda \times A_n(\lambda)$. If now consider momentum space to be the parameter space, the Berry curvature is:

$$\Omega_n = \nabla_k \times A_n(k) \tag{21}$$

The Berry curvature then behaves like a magnetic field [11] in momentum space. Using Stokes theorem:

$$\gamma_n = \oint_C d\lambda \cdot A_n(\lambda) = \int_S d^2k \cdot \Omega_n(k) \tag{22}$$

Where, S is the surface enclosed by the path C. We now consider the Brillouin Zone (BZ) of a 2D system, where the opposite edges of the BZ are equivalent. We can then perform the integral of $A_n(\lambda)$ around the edges of the BZ in a clockwise or anticlockwise direction to get the Berry phase, γ_{BZ} or -γ_{BZ}, depending on the direction. Since the opposite edges of the BZ are equivalent, the Berry phase acquired by the wavefunction is the same for both directions. This means that either the Berry phase is zero or it is an integer multiple of 2π, such that $e^{i\gamma_{BZ}} = 1$, and the wavefunction remains unchanged. And if we integrate over the entire Brillouin Zone, we get the first Chern number, C_n which is an integer:

$$2\pi C_n = \int_{BZ} d^2k \cdot \Omega_n(k) \tag{23}$$

Thouless et al. (1982) [34] showed that the Kubo formula for the Hall conductance can be used to show the quantization of Integer Quantum Hall effect. It was then shown by Kohmoto et al. (1985) [21] that the Chern number is the topological constant that determines the quantization of the Hall conductance, and the Hall conductance is given by:

$$\sigma_{xy} = \frac{e^2}{h} \sum_n C_n \tag{24}$$

Here, the nth band has the Chern number (C_n) and the sum is over all filled n bands.

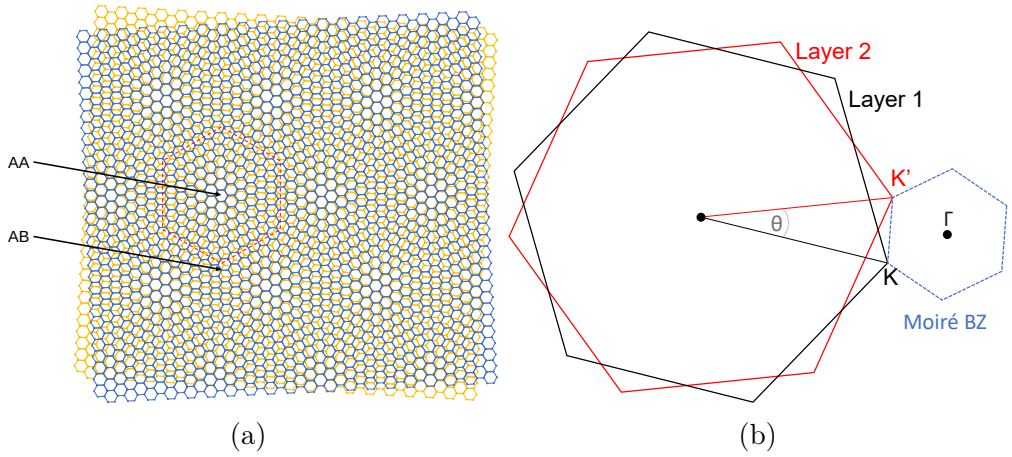

(a) (b)

Figure 4: (a) Moiré Superlattice with AA and AB stacking regions (b) Brillouin Zone of Moiré Superlattice

1.2.4 Band Structure Modulation by moiré superlattice

When two sheets of graphene are subject to small rotational misalignments, a moiré superlattice is formed. The moiré superlattice is a provides a periodic modulation of the potential landscape for the electrons in the graphene layers, with a period bigger than the lattice periodicity of the graphene. The moiré superlattice is thus used to modify the band structure. Near certain twist angles, the energy bands associated with the moiré superlattice become extremely flat, suppressing kinetic energy of the electrons [3]. For such regimes, the Coulomb interaction between them dominates, leading to Mott-like insulating behaviour at certain fillings of the moiré superlattice. These insulating states are called correlated insulating states, where the electrons effectively localize owing to the strong Coulomb interactions, despite the availability of free states in the band structure.

Starting from a tight-binding continuum Hamiltonian, Bistritzer and MacDonald (2011) [4] showed that the Dirac velocity at moiré superlattice Dirac point goes to zero at certain twist angle, leading to the formation of flat bands. This is because smaller Dirac velocity corresponds to a larger effective mass of the electrons, which supresses the kinetic energy of the electrons [3]. The angle where the Dirac velocity goes to zero is called the magic angle. The first magic angle for twisted bilayer graphene (tBLG) is around 1.1°. There are other magic angles at smaller and larger twist angles, but the 1.1° magic angle is the most studied, due to it being large enough to be experimentally accessible, while still yielding strong flat band conditions.

Chapter 2

Methods

2.1 Sample Preparation

In this section, we will describe how the samples were fabricated for this study.

2.1.1 Exfoliation of layered 2D materials

We start preparing the samples by isolating thin layers of 2D materials like graphene and hBN. This is done by mechanically exfoliating the materials from bulk crystals using the 'Scotch Tape' method. The dry exfoliation of the materials is very important step, as the presence of any contaminant at this stage will introduce disorder in the final device.

2.1.1.1 Graphene

Graphene is exfoliated from bulk naturally occurring graphite crystals. The graphite is cleaved using the 'Scotch Tape'. A piece of bulk graphite with a fresh surface is then put on the tape[36]. The tape is folded over the bulk crystal and is then unfolded to further exposes a fresh surface and cleave the graphite. This is process is reiterated until the tape is fully covered with graphite[12][13]. We will call this tape the 'mother-tape'. For the exfoliation of graphene, we directly press this mother-tape on a clean Si/SiO_2 substrate and peel it off (Fig. 5a).

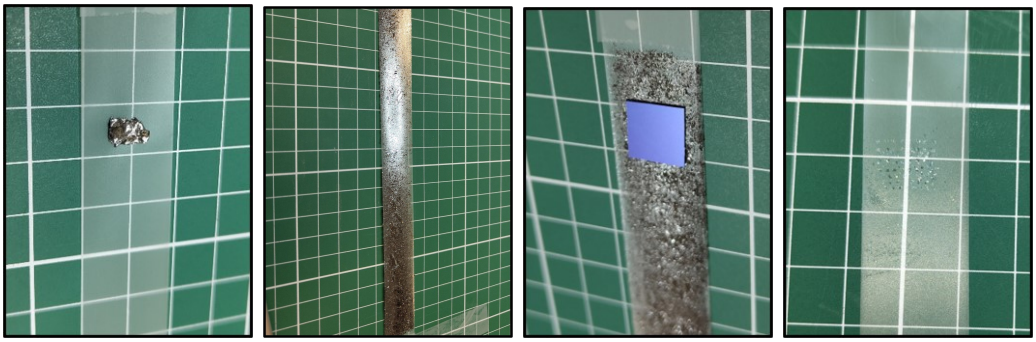

(a) (b) (c) (d)

Figure 5: Exfoliating of graphene and hBN: (a) Bulk graphite on tape (b) Exfoliated 'mother-tape' (c) graphene tape pressed to substrate (d) hBN 'mother-tape'

To obtain a higher yield of thin layers of graphene, we can first use oxygen plasma to clean the substrate and draw out any organic adsorbates on the surface of the SiO_2[16]. This will result in a greater yield of graphene on the substrate. After sticking the mother-tape on the substrate, we anneal the substrate at 110°C for a couple of minutes to improve the adhesion of the graphene to the substrate, by removing any trapped gasses between the graphene and the substrate[16]. The tape is then peeled from the silicon chip at a slow pace. This results in the cleaving of the graphene layers from the mother-tape which were in contact with the substrate. We do not want to transfer entire graphene flakes from the mother-tape, as this will result contamination from the adhesive of the tape. We only want to cleave a few layers of graphene that are in contact with the substrate.

2.1.1.2 Hexagonal Boron Nitride (hBN)

Just like graphene, atomically-thin hBN is also exfoliated from bulk hBN crystals. The exfoliation process is similar to that of graphene. The hBN is cleaved using the same 'Scotch Tape' method to expose a fresh surface. The tape is then folded over the hBN and peeled off to cleave the hBN. This is repeated multiple times to obtain thin layers of hBN on the tape until the tape is fully covered with hBN, to create the 'mother-tape'(Fig. 6c). A crucial difference from the exfoliation of graphene is that the hBN is prone to breaking into small pieces during the exfoliation process, so care must be taken to not overlap the hBN crystals on the mother-tape. Unlike graphene, we will not directly use the mother-tape and instead prepare a daughter-tape by sticking a clean piece of tape on the mother-tape and peeling it off. This daughter tape is then used to transfer the hBN to the substrate to obtain clean hBN flakes similarly to graphene.

2.1.1.3 Screening of the samples

After exfoliation, the samples are screened under an optical microscope to identify the flakes of graphene and hBN. The flakes are identified by their optical contrast with the substrate. To differentiate graphene flakes of different thicknesses, we use the optical contrast of the flakes on the substrate. The contrast of monolayer graphene is approximately 3%, while that of bilayer graphene is 6% and so on for our optical setup. For the fabrication of a twisted monolayer-bilayer graphene (tMBG) device, we need to start with a contiguous monolayer and bilayer graphene flake without apparent distortion (wrinkles, tears, etc.) as such a defect can add that can add an unknown additional twist to the system.

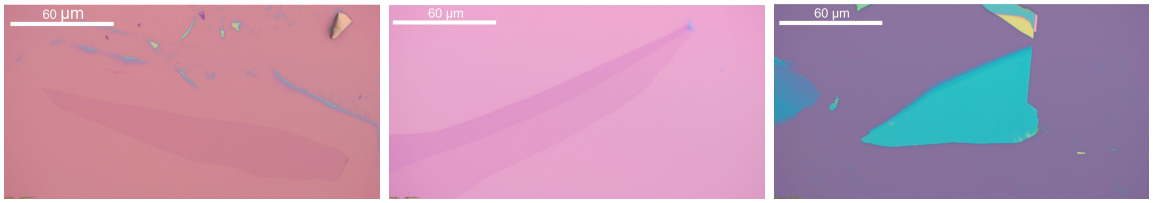

(a) (b) (c)

Figure 6: Screening of the samples: (a) Monolayer graphene (b) Monolayer and bilayer graphene (c) hBN

The hBN flakes are identified by their colour by comparing them with a pre-established colour chart. Homogenous flakes of hBN in the thickness range of 10-40 nm are selected for

the fabrication of the devices.

2.1.2 AFM lithography

To disconnect the monolayer and bilayer domains before heterostructure assembly, AFM (Atomic Force Microscope) lithography was used. We used Local Anodic Oxidation (LAO) [24] to oxidize the graphene layers in the desired pattern. The AFM tip is used to apply an AC excitation at 10V at 50KHz to the graphene layer in a humid environment of relative humidity around 60%. In Contact Mode, the tip is scanned over the graphene layer according to the designed pattern using the lithography module of the Park Systems AFM software.

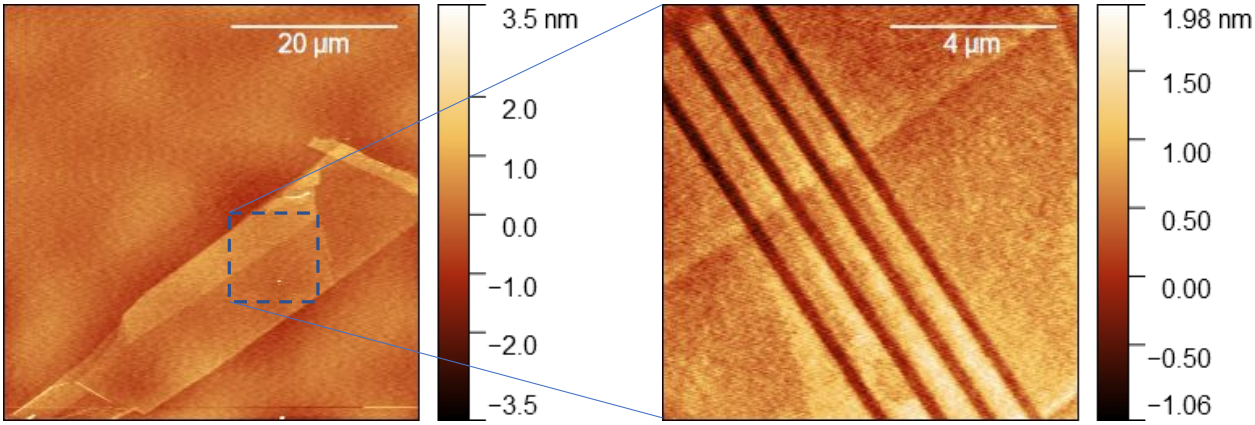

Figure 7: Left Panel: AFM image of graphene flake before AFM lithography. Right Panel: Zoomed in of graphene flake after AFM lithography

AFM-LAO works by locally oxidizing the graphene layers to form carbon oxides (CO_x) which are gaseous and leave behind no residue. But to initiate this reaction, the tip must go over the edge of the graphene flake where it encounters some dangling bonds which helps initiate the oxidation.

AFM lithography was also employed to pattern the top graphite (5-10 layers of graphene) gate for a Quantum Point Contact on Bilayer graphene. For a Quantum Point Contact device, the top gate needs to be split into four quadrants [8] so that we can apply different gate voltage to each quadrant, so that we can gate the device in a way that the potential landscape is different in each quadrant. This however presents a problem, because to realise this device, as a pattern needs to be made that is completely contained in the graphene flake. This makes it very difficult to initiate the oxidation reaction as the tip cannot go over the edge of the flake (where it encounters the dangling bonds) to initiate the oxidation. By

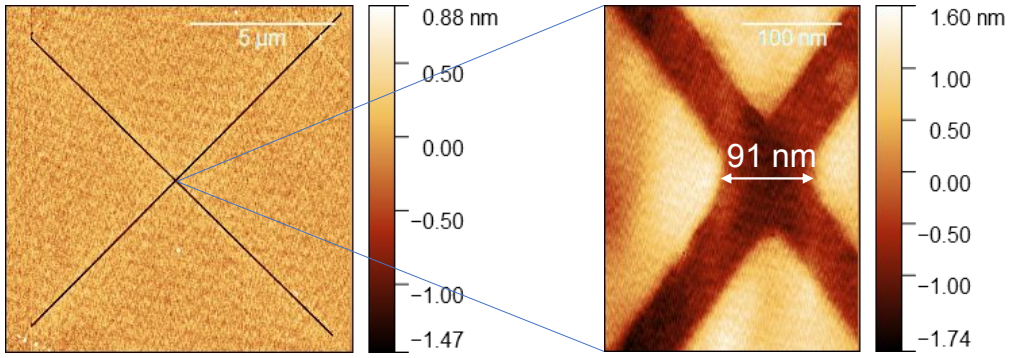

(a)

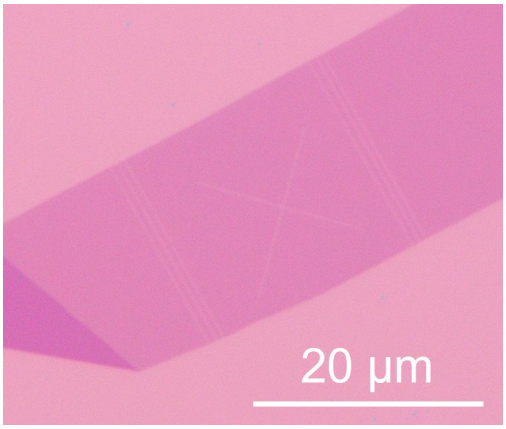

(b)

Figure 8: AFM lithography: (a) AFM image after lithography (b) Optical image after lithography

trial and error, we found that the oxidation reaction can be initiated by patterning a dot on the flake, possibly because of better connection between the tip and the flake at some intermediate regime while the AFM tip approaches or retracts. But this seems to occur only once in three attempts. So, we use a 'brute-force' method to create several (3-4) dots by AFM lithography at the same location. This 'burns' a small hole in the flake, and then we can use the dangling bonds at the hole to initiate the oxidation in a desired pattern that is completely contained in the flake(Fig. 8a). This process varies between AFM setups and the exact parameters need to be optimised for each setup. We used a Park Systems NX-20 AFM with a ElectriMulti75-G cantilever with a conductive tip coated with Cr-Pt.

2.1.3 Transfer of 2D materials

The transfer of the 2D materials is done using the dry transfer method [38] [12]. To begin with, the images of the selected flakes are added to a PowerPoint presentation to make a rough outline of the stacking process. A 'pick-up' slide is prepared by putting a piece of PDMS (Polydimethylsiloxane) on a glass slide and then covering it with a thin PC (Poly(Bisphenol A carbonate)) film. The PC film is prepared by first dissolving some PC in Chloroform and transferring a small amount of this solution on a clean glass slide. Another slide is slid across the first one to smear the PC into an even film. The glass slide is then allowed to dry to let the Chloroform evaporate. The PC film is then peeled off using a piece of tape with a hole in the center and placed on the PDMS slide. This is the 'pick-up' slide (Fig. a), which is then annealed at 140°C for 10 minutes to make sure the PC film sticks to the PDMS and to remove any trapped gasses between the PC film and the PDMS. The 'pick-up' slide is then used to pick up the identified flakes of graphene and hBN from the substrate sequentially. This process is called 'stacking' of 2D materials via dry transfer method.

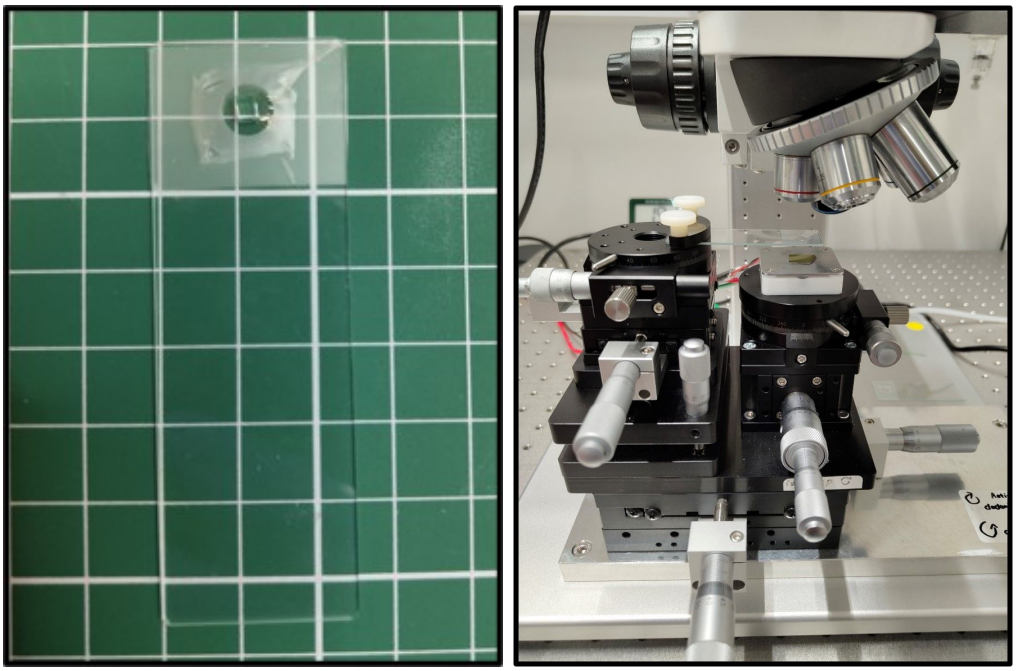

(a) (b)

Figure 9: Transfer of 2D materials: (a) 'Pick-up' slide (b) Transfer stage

The transfer of the 2D materials is performed using a transfer stage (Fig. 9b). The 'pick-up' slide is attach to a XY manipulator stage, while the substrate (with the target

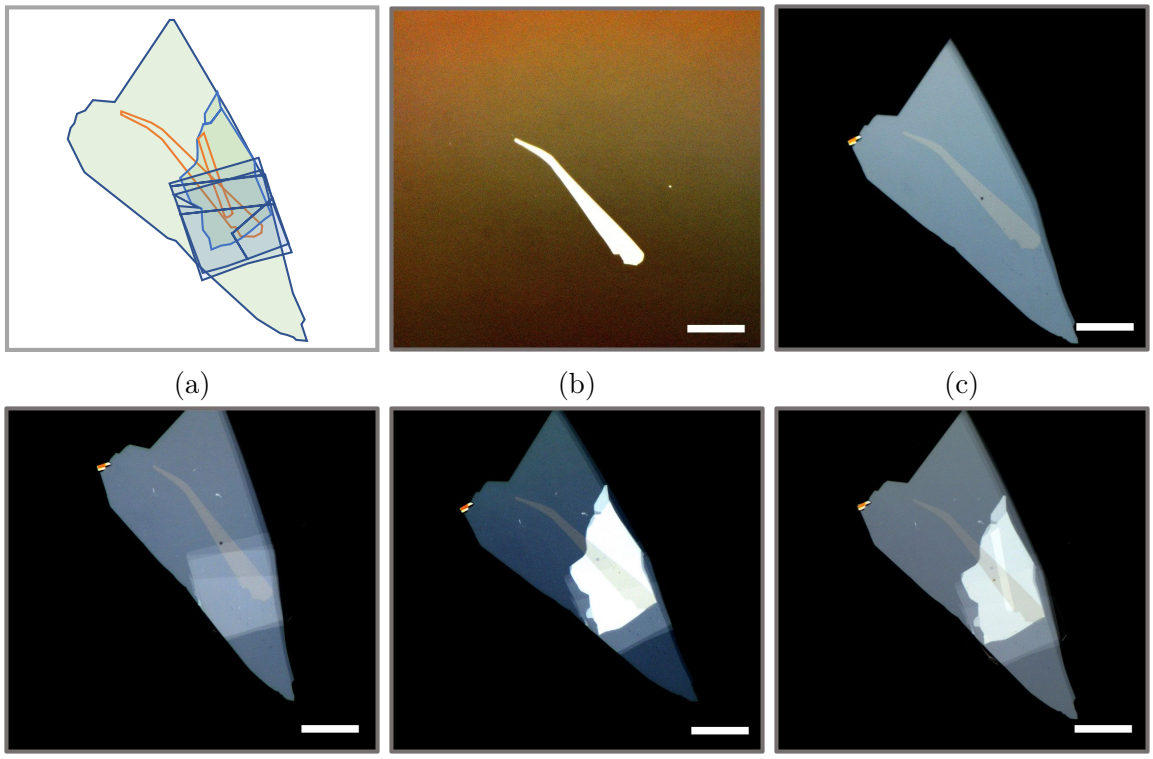

Figure 10: Stacking of 2D materials: (a) stack schematic (b) top Gate (c) top hBN (d) bilayer and monolayer graphene (e) bottom hBN (f) bottom gate. Scale bar is $20\mu m$

flake) is placed on XYZ manipulator stage. XYZ manipulator stage also has a rotation stage and heating element to anneal the substrate.

For the dual gated twisted monolayer-bilayer graphene (tMBG) heterostructure, the stacking order is as follows (top to bottom): top graphite gate, top hBN dielectric, bilayer graphene, monolayer graphene, bottom hBN dielectric, bottom graphite gate. The graphite layers are used to apply gate voltages, while the hBN layers are used to encapsulate the graphene layers and act as an atomically flat substrate for graphene as well as a gate dielectric. For most of the devices made in this study, all the layers were stacked at a relatively high temperature: 80°C - 110°C. This was done to improve the homogeneity of the device during the stacking process[13]. All the steps of the stacking process are shown in Fig. 10.

After all the layers have been successfully picked up, the stack on the 'pick-up' slide is then aligned with a pre-patterned substrate with gold pads for electrical contacts (Fig. 11a). After positioning the stack at the center of the gold pads, the substrate is laminated at 90°C - 110°C. After lamination, temperature is steadily increased to 180°C, beyond the glass

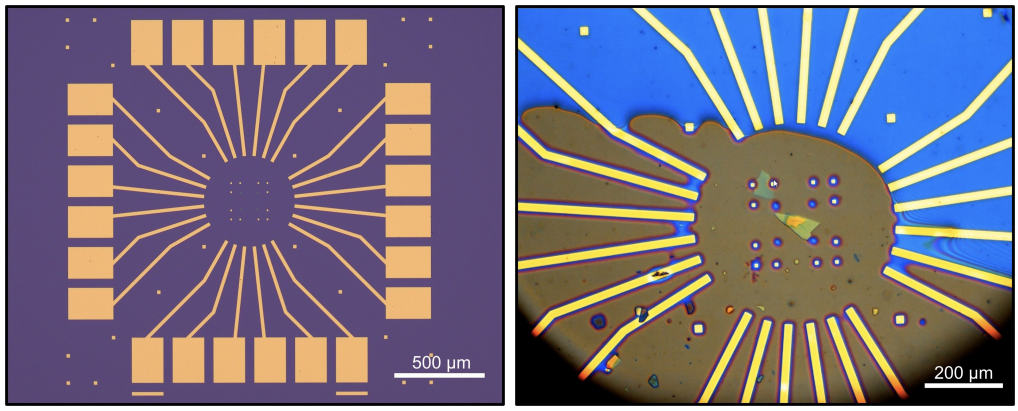

(a) (b)

Figure 11: Releasing the stack: (a) Silicon chip with gold pads (b) Stack on the silicon chip

transition temperature for the PC film (around 148°C). This results in the PC film becoming soft and detaching from the PDMS stamp, thereby releasing the stack on the substrate (Fig. 11b). The PC film is then dissolved by soaking the silicon chip in Chloroform for a long duration (half a day).

This stacking process was also used make a Quantum Point Contact (QPC) on Bernal bilayer graphene. As described earlier, the top gate for the QPC device was patterned using AFM lithography. For this stack, we started with a top hBN layer which acts an atomically flat substrate for the patterned top gate. After picking up the top gate on the hBN layer, an AFM scan was performed on the stack (on the 'pick-up' slide) to ensure that the patterned gap in the top gate, survived the transfer process. This also demonstrates the self-cleaning properties[12] [8] of 2D materials assembly, as residues seen after AFM lithography (Fig. 12a), were not present after the transfer process (Fig. 12b).

After that another layer of hBN was picked up, followed by bilayer graphene, bottom hBN and the bottom graphite gate. They were aligned such that electrical contacts can be made to each quadrant of the top gate, individually. The four parts were electrically disconnected from each other by etching away the part of graphite that was connecting them. After successfully releasing the stack on a pre-patterned substrate, the next step is to shape the device into a Hall bar like geometry and make electrical contacts. These steps are described in the next section.

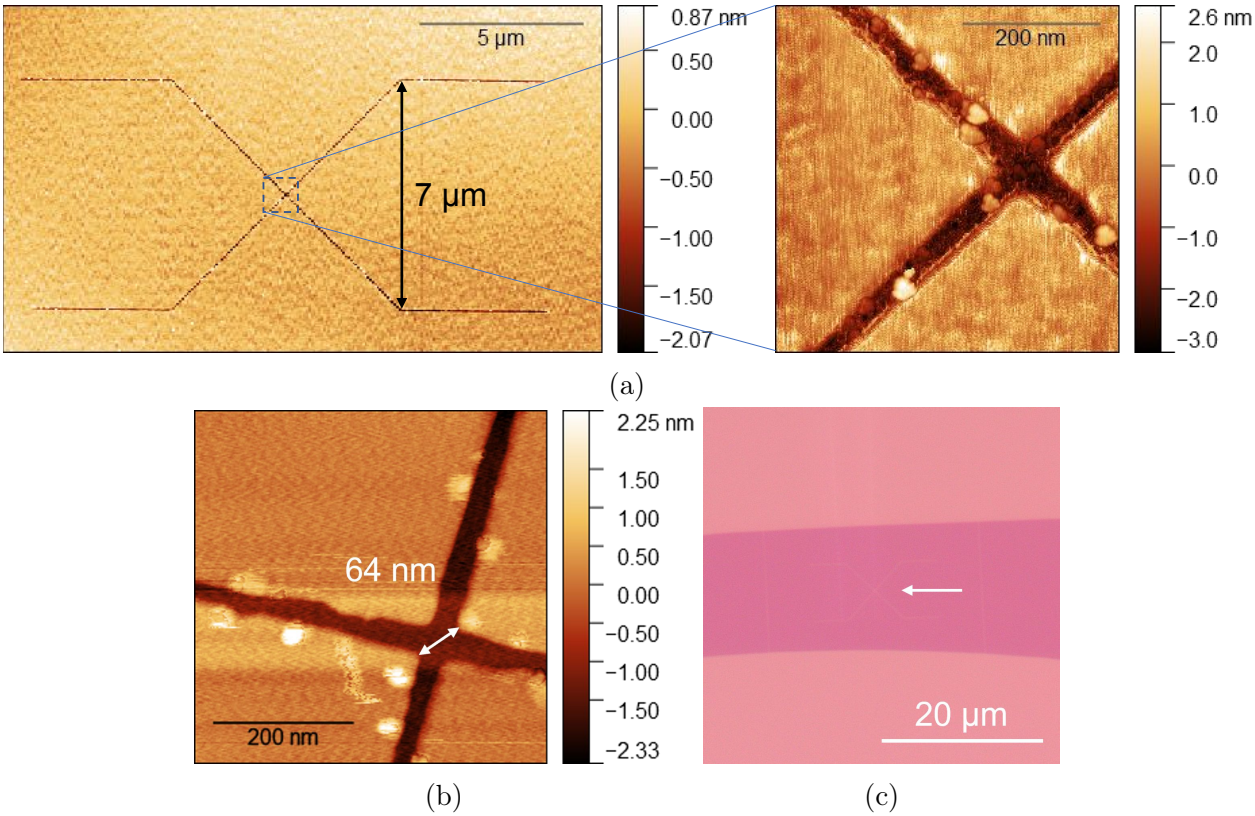

Figure 12: Patterning of graphite gate: (a) Left: AFM lithography on few layers graphite; Right: Zoomed-in image showing some lithography residue (b) After picking up the graphite gate on hBN (c) Optical image of the patterned top gate with faintly visible cuts.

2.2 Device Fabrication

To turn a stack of 2D materials into a functional device, we use nano-fabrication tools in the cleanroom to 'process' the stack. We begin by defining a Hall bar on the stack using Electron Beam Lithography (EBL). Then the stack is shaped into the Hall bar by etching. And finally contact metal is deposited, and the device is wire-bonded on a sample holder to complete the device.

2.2.1 Electron Beam Lithography (EBL)

The first step in the EBL process is to spin-coating an E-beam resist on the Silicon chip. We two layers of PMMA (Poly(methyl methacrylate)), one layer of 600K (600,000 gm/mol) followed by another layer of 950K (950,000 gm/mol). Each layer is spun on the chip at 3000

rpm, followed by 5 minutes of annealing at 180°C. A Hall bar design is made using AutoCAD software, and an E-Beam writer (Raith EBPG) is used to write the design on the Silicon chip. A solution of water and Isopropyl Alcohol (IPA) (3:1 by weight) is used a developer for the E-beam Resist.

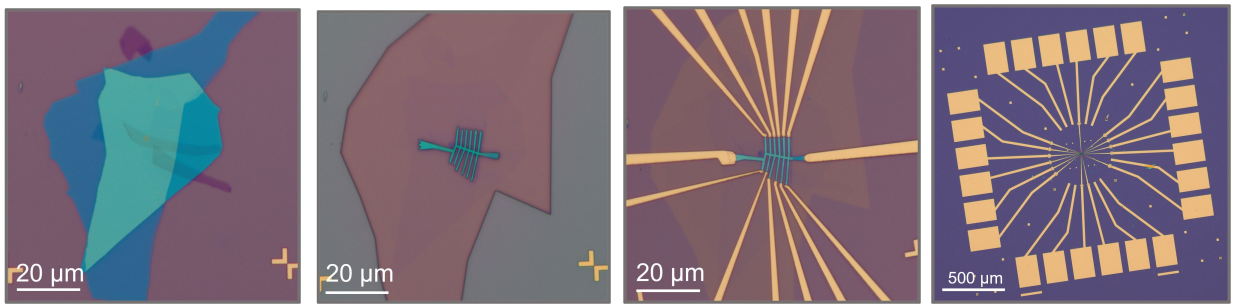

(a) (b) (c) (d)

Figure 13: (a) Stack assembled on silicon chip (b) Stack after etching (c) Contacts defined by EBL and E-beam evaporation (d) Final device with gold pads

2.2.2 Inductively Coupled Plasma (ICP) Etching

After defining a Hall bar mask on the stack, ICP Reactive Ion Etching (RIE) is used to uni-directionally etched away the regions not protected by the mask defined by EBL. A mixture of O_2 (Oxygen) and CHF_3 (Fluoroform) is used for etching.

2.2.3 Metal Deposition

After etching, PMMA mask is dissolved in Acetone, the contacts to the Hall bar are defined in the same way using EBL. Contact metal is then deposited on the silicon chip using E-beam evaporation. We use a stack of Chromium (3nm), Palladium (15 nm) and Gold (150nm) as the contact metal.

2.2.4 Sample Mounting

The silicon chip is then diced to fit the sample holder. The gold pads on the silicon chip are wire-bonded to the sample holder to make electrical contacts. The sample is now ready to be loaded into the cryostat for measurement.

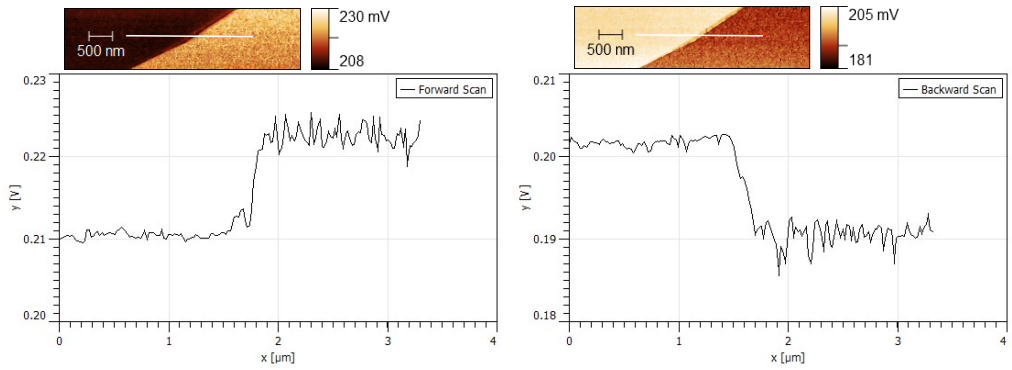

(a) (b)

Figure 14: LFM Scans on Bilayer graphene on SiO_2: (a) Forward scan (b) Backward scan

2.3 Lateral Force Microscopy

Lateral Force Microscopy (LFM) is a measurement configuration in AFM Contact mode, that allows one to map the dynamic friction between the AFM tip and the scanning surface. This can be used to measure tiny electrostatic potentials on the surface on the sample that otherwise cannot be resolved by measuring the height profile in the Z direction. This mode works by recording the lateral displacement of the laser spot on cantilever as it scans the sample. LFM scans give us complementary information in forwards and backwards scanning directions (Fig. 14).

This technique was used to attempt the imaging of moiré superlattice in tBLG. The moiré period for the target twist angle of around 1°, is in the range of 10-20nm. This makes it imaging the moiré superlattice especially difficult, due to environmental noise. We have however been able to indirectly observe the moiré superlattice by analyzing the noisy data, which will be described in the next chapter. We have also measured the noise floor of the AFM through zero scans. Efforts are being made to improve the noise floor of the AFM to make the imaging of the moiré superlattice more reliable.

2.4 Measurement Setup

All the data was collected in an Oxford Instruments Teslatron PTR (Pulse Tube Refrigerator) cryostat with a base temperature of 1.5K. It has a superconducting magnet that go up to 8T. The devices are shaped like a Hall bar. The electrodes at each end of the Hall bar are connected to both gates of the device (labelled V_t and V_b respectively in Fig. 15).

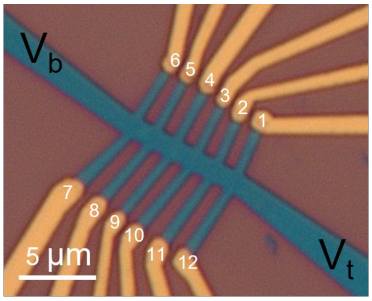

Figure 15: Hall bar geometry

The electrodes labelled 1-12 are connected to the channel material, i.e., the graphene layers. DC biases are applied to the top and bottom gates[36] using a DAC (Digital to Analog Converter). A pair of electrodes are used as source and drain, with an A.C. excitation applied to the source at 17.77 Hz and the current is measured at the drain after an amplification of 10^{-6} AV^{-1}. The voltage is then measured between a pair of electrodes with a gain of 100 using a Lockin-In detection. Both current and voltage are measured using SRS 830 lock-in amplifiers. The resistance can now be obtained by simply dividing the voltage by the current. The Hall resistance (R_{xy}) is obtained by measuring the voltage between opposite electrodes (electrode 2-11 for example) and the longitudinal resistance (R_{xx}) is obtained by measuring the voltage between adjacent electrodes (electrode 1-2 for example). The measurement schematic is shown in Fig. 16.

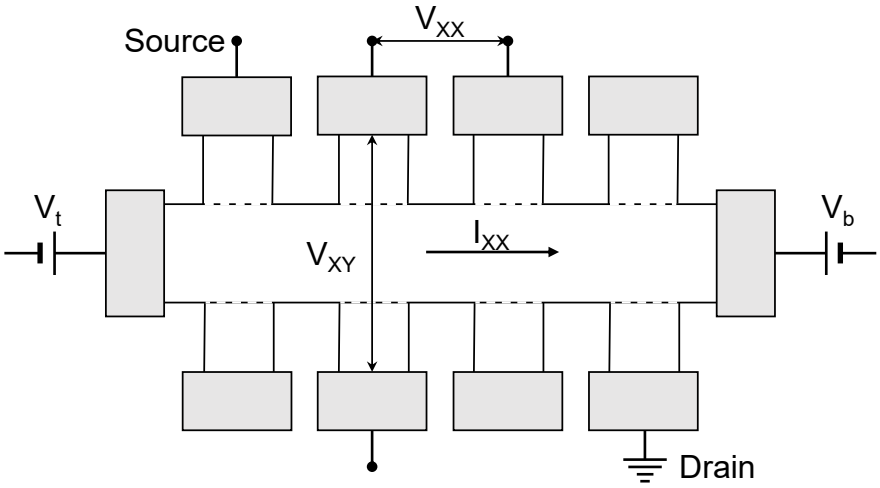

Figure 16: Measurement Schematic

Chapter 3

Results and Discussion

3.1 Phase Diagrams

The extensively studied system of tBLG, has reports of superconductivity[6], orbital magnetism[33], and correlated insulating states[5]. The study of tMBG however can provide new insights into these phenomena because the band structure can be modified by applying a vertical electric field. This is because the parabolic dispersion of AB stacked bilayer graphene can be better tuned by gating[40], while the linear dispersion of monolayer graphene remains unaffected. The band structure of tMBG can be modified by the twist angle, the vertical electric field and the carrier density.

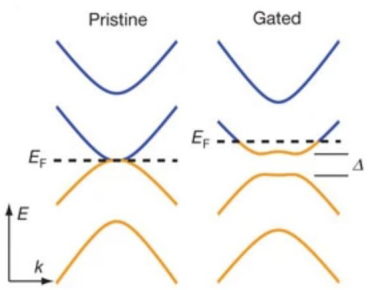

Figure 17: Opening of bandgap in bilayer graphene[40]

To see this in practice, we make a dual-gated twisted monolayer-bilayer graphene (tMBG) device. The gates are used to apply different voltages to tune the vertical electric field (also called displacement field) and the carrier density. The device schematic is as shown in figure 18a.

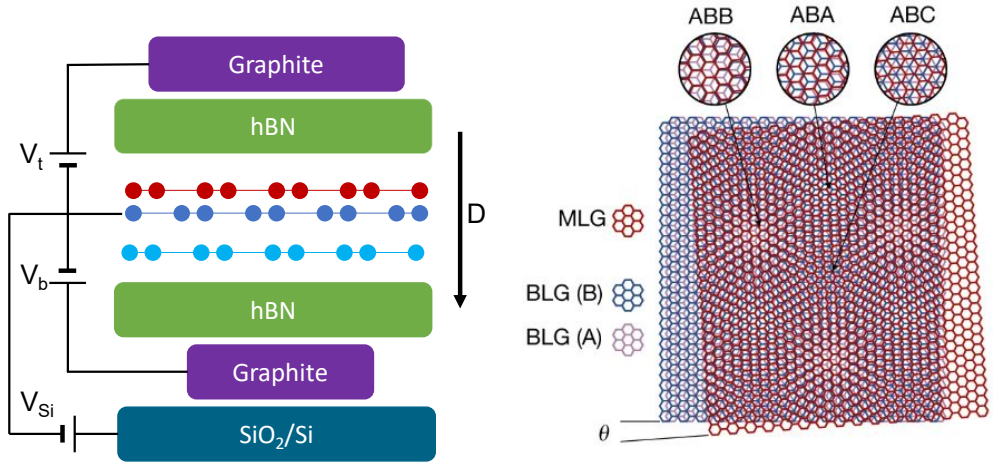

(a) (b)

Figure 18: (a) Schematic of tMBG device (b) Moiré superlattice in tMBG[29]

Due to the presence of a third layer[15] as compared to twisted bilayer graphene (tBLG), the moiré superlattice in twisted monolayer-bilayer (tMBG) shows a more complex stacking pattern, with regions of ABB, ABA and ABC stacking order. Each of these local stacking configurations can have different band structure properties that influences how carriers move in the device. The presence of the bilayer graphene, makes the band gap tunable with displacement field. All of these factors contribute to a richer phase diagram in tMBG.

In tMBG graphene, the magic angle for the emergence of flat bands was predicted to

be in the range of 0.88°- 1.5°[30]. The existence of Quantum Anamalous Hall Effect was also predicted at one quarter and three quarters filling factors in a range of twist angles 1°-1.4°[30]. This has subsequently been observed experimentally[29]. We will now discuss the data from the tMBG devices made in this study.

3.1.1 Transport measurements

A total of 10 tMBG stacks were made, out of which 6 have been processed and measured. The summary of all the devices is as follows:

Label	**Measured twist angle (°)**	**Target twist angle (°)**	**Notes**
tMBG4	-	1.5	Low temperature stacking; Relaxed twist angle
tMBG5	-	1.4	High temperature stacking; Relaxed twist angle
tMBG6	-	1.4	High temperature stacking; Device not processed
tMBG7	-	1.4	High temperature stacking; Device damaged during processing
tMBG8	-	1.4	High temperature stacking; Relaxed twist angle
tMBG9	1.38	1.4	High temperature stacking
tMBG10	1.9	1.4	High temperature stacking; Large twist angle
tMBG12	0.4-0.6	1.4	High temperature stacking; Small twist angle
tMBG13	-	1.35	Intermediate temperature stacking; Yet to be measured
tMBG15	-	1.35	Intermediate temperature stacking; Yet to be measured

Table 1: Twisted Monolayer-Bilayer Graphene devices

Relaxed twist angle in this context means, either the angle has reduced to zero after the transfer process, or the angle is very large (>2°) and the layers are decoupled. In both of these cases it is difficult to approximate the twist angle from transport measurement. Since the stacks in this study were made at a high temperature with the goal of improving homogeneity, there is a greater variability in the twist angle. This is because while stacking at high temperatures, the chances of the layers sliding over each other increases, leading to a deviation from the target twist angle. We will begin by discussing the data from tMBG9, which has a twist angle of 1.38°, and then look at the data from other devices, that aren't near the magic angle.

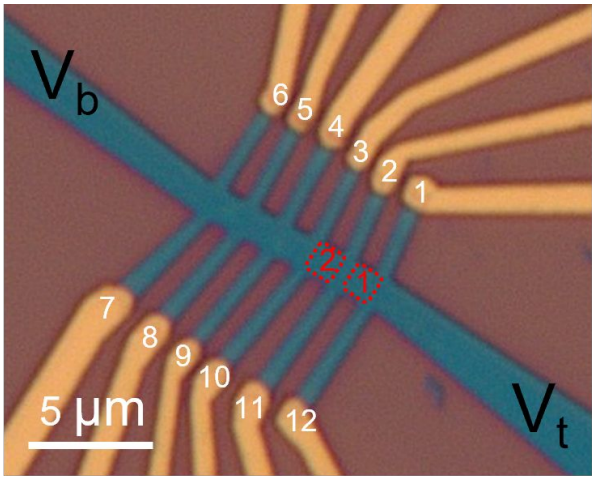

Figure 19: Optical image of tMBG9, with the gate electrodes labelled V_t and V_b for top and bottom gates respectively

3.1.1.1 tMBG9

This device was measured in a cryostat at the base temperature of 1.5K. The details of the measurement configuration described in the previous chapter. The image of tMBG9 is shown in Fig. 19. The device was measured in the Hall bar configuration, with the current flowing from the source to the drain, and the Hall voltage measured across the Hall bar. Maps of R_{xx} and R_{xy} were measured by varying the voltage of the top and bottom gates[2], and plotted against the carrier density (on X axis) and the displacement field (on Y axis).

Fig. 20b & 20a, show the R_{xy} and R_{xx} maps for section 1 and 2 (marked in red in Fig. 19). X-axis and Y-axis represents carrier density and displacement field respectively, and the resistance is plotted as a colour scale. The maps show the formation of insulating states at certain carrier densities. At zero carrier density, we see an insulating state at some non-zero displacement field. This corresponds to the gapped phase at the charge neutrality point (CNP) at non-zero displacement field. At the negative displacement field, we see the formation of an insulating state at around the carrier density of $2 \times 10^{12} cm^{-2}$. This corresponds to a correlated insulating state at some partial filling of the moiré superlattice. And then around the carrier density of $4 \times 10^{12} cm^{-2}$, we see the formation of another insulating state, which is the band insulator at the full-filling of the moiré superlattice.

We also notice some noisy streaks in the phase diagrams that run along a certain direction. These are due to single gated regions in the device, where only the top or the bottom gate is effective in gating the device. These features do not affect the overall phase diagram,

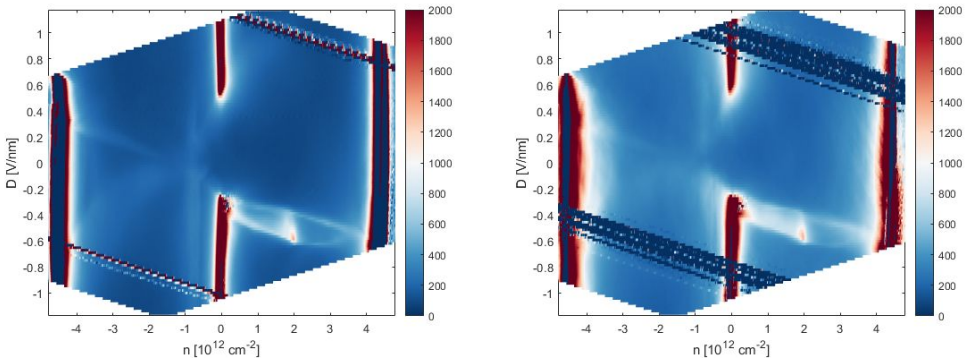

(a) (b)

Figure 20: R_{xx} and R_{xy} plotted against carrier density and displacement field (a) R_{xx} at zero field for contacts 11-12 (section 1) (b) R_{xx} at zero field for contacts 10-11 (section 2)

but they can cause trouble while measuring some features if these streaks appear in the region of interest. If this happens, a bias on the silicon gate (Fig. 18a) can be used to shift these streaks out of the region of interest.

The X-axis can be scaled to the filling factor by dividing the carrier density by the carrier density corresponding to fully-filled moiré band(superlattice carrier density (n_s)) and multiplying by 4 because there are four charge carriers per moiré unit cell at full-filling. The filling factor (ν) is:

$$\nu = 4\frac{n}{n_s}$$

The n_s in this case is around 4.3 $\times 10^{12} cm^{-2}$. The phase diagrams after scaling the X-axis are shown in Fig. 21. From this plot we can see the correlated insulator at half filling ($\nu = 2$) and the band insulators at full-filling ($\nu = 4$). There is some asymmetry in the phase diagram as the insulating state at full-filling on electron and hole doping sides don't occur at identical filling factors. This can be attributed to moiré disorder in the device, which leads to a distribution of twist angles in the device around the measured twist angle. This leads to smearing out of some features in the phase diagrams as the transport signal from competing twist angle domains are averaged out.

Fig. 21b shows the R_{xy} map for contacts 2-11 (section 2) at +900mT. The blue colour (negative Hall resistance) in the map represents the negatively charged electron-like carriers, while the red colour (positive Hall resistance) represents the positively charged hole-like carriers. We see a change in the Hall sign at a few different places in the map. We see a trivial change in the Hall sign at the CNP, as for $\nu < 0$ the transport is dominated by hole-like carriers, while for $\nu > 0$ the transport is dominated by electron-like carriers. At

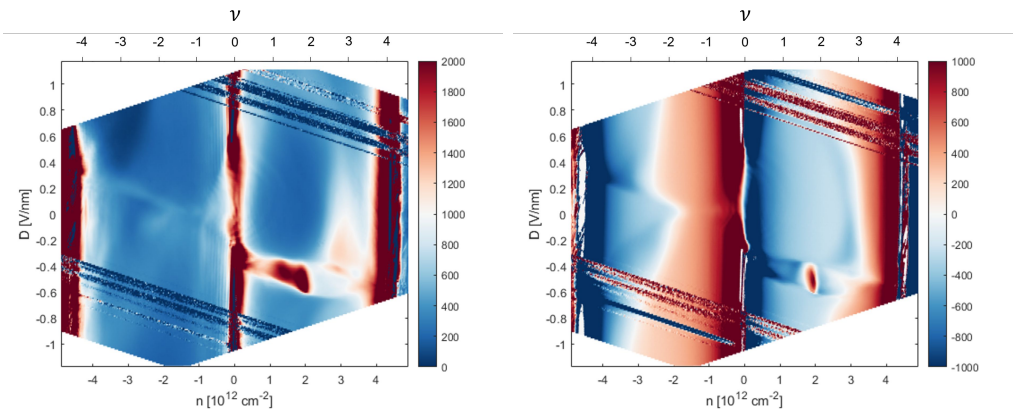

(a) (b)

Figure 21: R_{xx} and R_{xy} plotted against carrier density (and filling factor(ν) marked on the top axis) and displacement field (a) R_{xx} at +900mT (b) R_{xy} at +900mT

the band insulating state at full-filling ($\nu = \pm 4$), the Hall sign changes indicating that all states in the current moiré mini-band have been exhausted. Any additional carriers must occupy the next band which will have an opposite curvature leading to a change in the carrier type. At the insulating state at hall-filling ($\nu = +2$) around D = -0.5 V/m, the Hall sign changes from hole-like to electron-like indicating a switch in the nature of the carriers at the insulating state. This change happens at an interaction induced band gap opening at hall-filling of the moiré superlattice, as the Fermi level crosses the band gap from hole-like sub-band to electron-like sub-band, as seen in Fig. 23a. All of these changes in the Hall sign are consistent with insulating states observed in the longitudinal resistivity (Fig. 21a).

However, we also see a change in the Hall sign, at all displacement fields on hole and electron doping regimes that cannot be explained by the existence of a gapped band structure. This can be attributed to a van Hove singularity [37] (vHS) in the density of states at certain carrier densities. The occurrence of vHS is attributed to the presence of a saddle point in the band structure, which in a divergence of the density of states. In monolayer graphene, vHSs occurs at a large distance from the Dirac point, making it inaccessible by gating in transport measurements. However, when two layers of graphene are stacked with an angle between them, the positions of the saddle points in the moiré BZ can be tuned by the twist angle making them accessible by gating. The two saddle points in a twisted graphene system can be seen in Fig. 22, both at positive and negative energies in the band structure. This was initially observed in twisted bilayer graphene using Scanning Tunneling Microscopy (STM) [23].

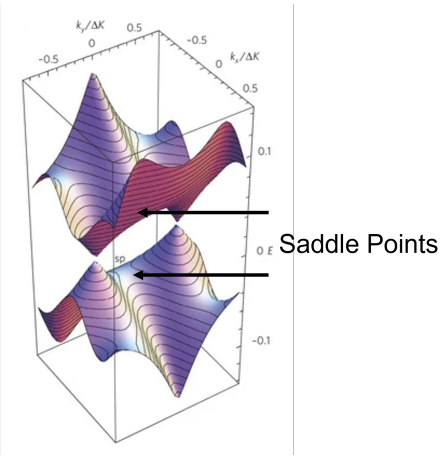

Figure 22: Saddle points in the Energy-momentum dispersion of twisted graphene layers [23]

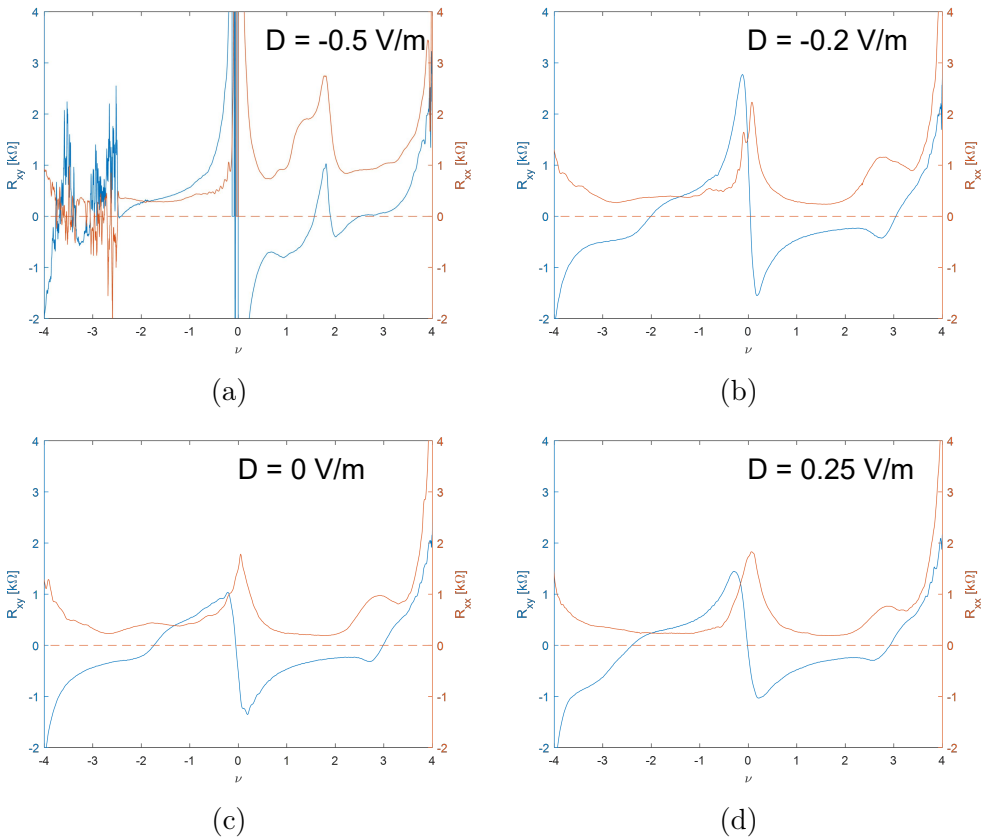

Figure 23: R_{xx} and R_{xy} plotted against filling factor and displacement field (a) R_{xx} at +900mT (b) R_{xy} at +900mT

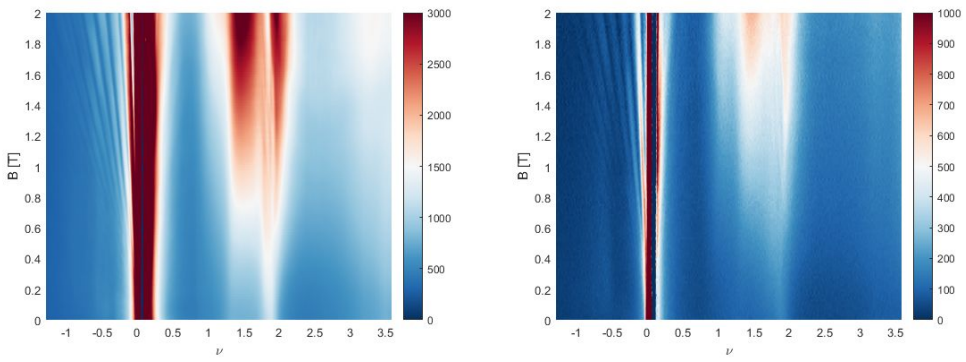

(a) (b)

Figure 24: Landau fan diagram for tMBG9; R_{xx} plotted against filling factor and magnetic field at fixed D = -0.53 V/m (a) Section 1 (b) Section 2

From the phase diagrams in Fig. 21b, we see that the Hall sign changes at certain carrier densities on that depends on the displacement field. This agrees with the existence of vHS in the density of states and we see this when the R_{xy} (shown in blue in Fig. 23) crosses zero at a distinct carrier density in the line-cuts at different displacement fields (Fig. 23b, Fig. 23c & 23d). This change in the Hall sign at the vHS is also accompanied by a small peak in the R_{xx}, which is consistent with the change in sign of the curvature of the band structure near the saddle point, leading to low carrier mobility as the Fermi level cross the saddle point. This agrees with the observation of vHS at comparable twist angles in twisted monolayer-bilayer graphene[39].

We also performed magneto-transport measurement on this device, and recorded Landau fan diagrams (Fig. 24) by changing the magnetic field at a constant displacement field, and plotting R_{xx} against the carrier density and the magnetic field. We see the formation of periodic low resistance states at certain filling factors due formation of Landau levels consistent with Quantum Hall Effect. This data can be used to estimate the twist angle of the device.

Twist angle extraction is done by fitting the low resistance in-gap states (Fig. 25) in the Landau fan diagram using the Streda formula (Eq. 25), which relates the filling factor to the magnetic field and the carrier density:

$$\nu = \frac{h}{e}\frac{\partial n}{\partial B} = \frac{\partial n}{\partial B/\Phi_0} \tag{25}$$

$$n = \frac{C_g}{e}V_g \tag{26}$$

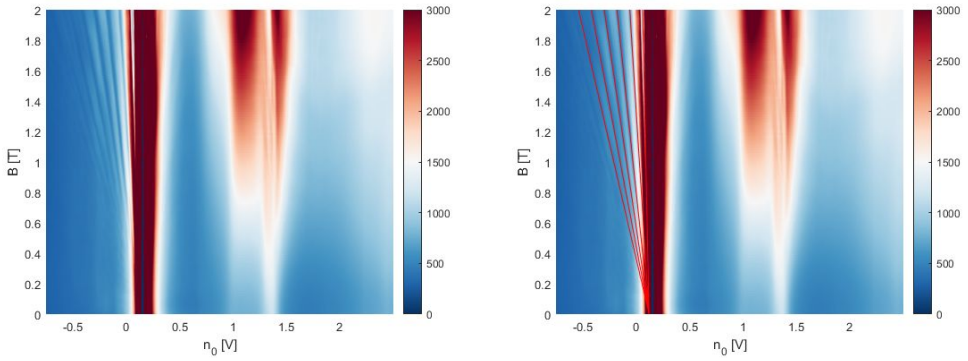

(a) (b)

Figure 25: Fitting Landau fan diagrams using Streda formula; R_{xx} plotted against gate voltages and magnetic field at fixed D = -0.53 V/m (a) Before fitting (b) After fitting

This can be arrived at from the expression of the Hall carrier density(17). From the slope of the Landau fans, we can obtain the relationship between carrier density and gate voltage[2]. This scaling factor is just the capacitance of the device in a simple parallel plate capacitor model. Using this scaling factor(C_g), we can convert the gate voltage to carrier density and displacement field. The twist angle can then be extracted by finding superlattice carrier density[2], n_s and using the following formula to find the twist angle:

$$n_s = \frac{4}{A_{moir}} = \frac{8\theta^2}{\sqrt{3}a^2} \tag{27}$$

Where, A_{moir} is the size of the moiré unit cell[11], θ is the twist angle, and $a = 2.46$Å is the periodicity of graphene. The size of the moiré unit cell is:

$$A_{moir} = \frac{\sqrt{3}}{2}\lambda^2 = \frac{\sqrt{3}}{8}\frac{a^2}{\sin^2(\theta/2)} \approx \frac{\sqrt{3}a^2}{2\theta^2} \tag{28}$$

where we have used the small angle approximation, $\sin(\theta) \approx \theta$ for small twist angles. Here, λ is the moiré period, which is related to the twist angle by

$$\lambda = a/\sin(\theta/2) \tag{29}$$

The twist angle for tMBG9 was found to be about 1.38°, which is close to the designed angle of 1.4°.

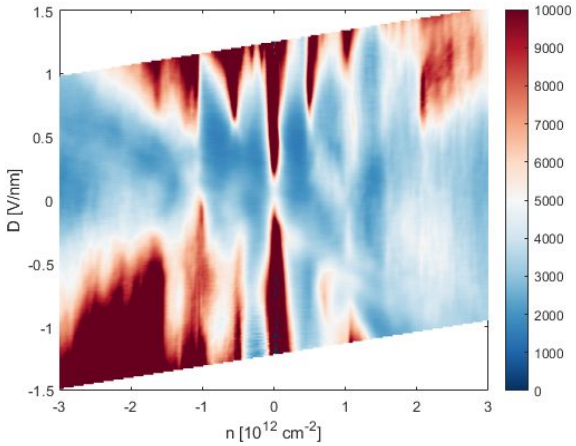

Figure 26: R_{xx} plotted against carrier density and displacement field for tMBG12

3.1.1.2 tMBG12

The twist angle for this device was approximated to be 0.4-0.6°, near the second magic angle. The phase diagram (Fig. 26) shows the formation of insulating states at certain carrier densities. However, the insulating states are not as well-defined, and due to disorder in the device, the features are smeared out. These insulating states seem to be correlated insulating states corresponding to partially filled superlattice. Since this device has a lot of twist angle disorder, there are several competing domains with different twist angles, leading to a smearing out of the features in the phase diagram. The Landau fan diagrams (Fig. (Fig. 27)) show very faint quantum oscillations due to the disorder in the device. As such calculating the exact twist angle from this data is difficult. We can however estimate the twist angle by roughly fitting the Landau fans and calculating the carrier density at for different insulating states, since we don't know which insulating state corresponds to full-filling due to the contributions from different domains in the transport measurement. The twist angle was therefore estimate to be in the range of 0.4-0.6°.

3.2 Imaging moiré superlattice

We tried to use Lateral Force Microscopy (LFM) to image the moiré superlattice in tBLG[17]. The sample was prepared by assembling an open-face tBLG on hBN, with a twist angle of 1.1°(Fig. 29). The sample was then scanned in LFM mode, as described in the previous chapter. From the intended twist angle of 1.1°, we would expect a moiré period of

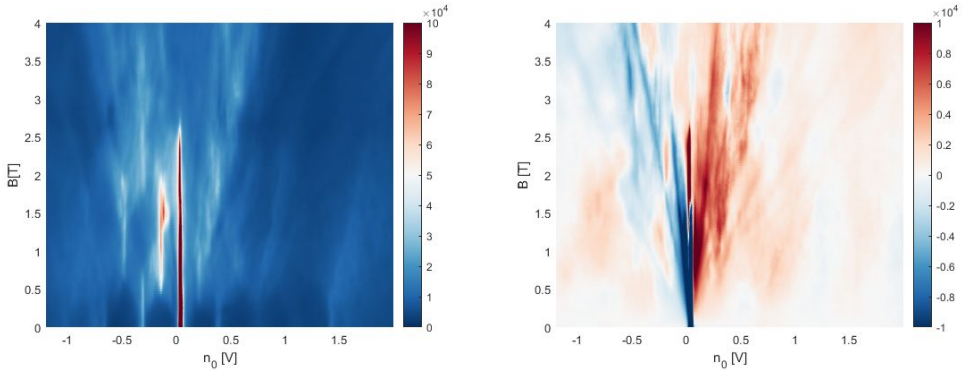

(a) (b)

Figure 27: Landau fan diagrams (a) R_{xx} plotted against magnetic field and carrier density (b) R_{xy} plotted against magnetic field and carrier density

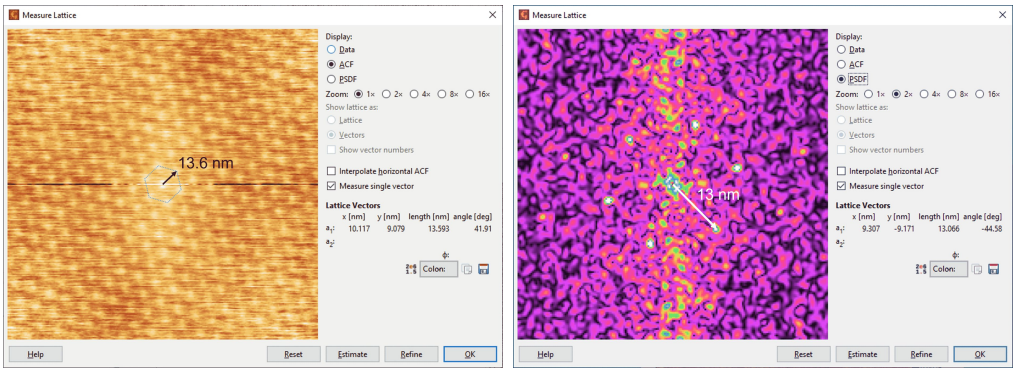

(a) (b)

Figure 28: (a) Auto Correlation Function of the LFM data (b) Power Spectral Density Function of the LFM data

around 12.8 nm, using Eq. 29. If we account for small twist angle variations in the range of $\Delta\theta = \pm 0.1°$ (since the sample was prepared at room temperature), then we expect, the period to be in range of 14.1 nm to 11.7 nm.

The LFM data however doesn't reveal any periodic pattern corresponding to the moiré superlattice. This is because the signal-to-noise ratio in the LFM channel is not high enough to resolve the moiré superlattice clearly. Upon further analysis of the raw LFM data, we found that there is indeed a periodic pattern in the data, that can be extracted by calculating the Auto Correlation Function (ACF) of the data in real space, and the Power Spectral Density Function (PSDF) in the reciprocal space. The ACF and PSDF are shown in Fig. 28. The ACF shows a periodic pattern with a period of around 14 nm, while the PSDF shows

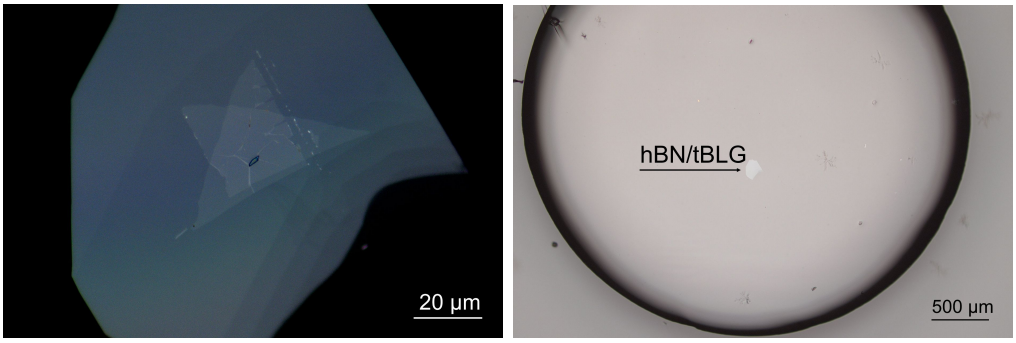

(a) (b)

Figure 29: (a) High contrast image of twisted bilayer graphene on hBN (b) hBN with tBLG on PDMS/PC stamp

a period of around 13 nm. This is consistent with the expected moiré period for the twist angle of the sample. The data analysis was done using the Gwyddion[27] software, which has built-in functions to calculate the ACF and PSDF of the data to extract the periodic patterns.

This is an indirect observation of the moiré superlattice, as the LFM data itself doesn't show a clear periodic pattern. Nevertheless, this demonstrates the potential of LFM to image the moiré patterns at abmient conditions, which can be very useful in screening of local twist angle disorder in devices.

3.3 Quantum Point Contact on Bernal Bilayer graphene

Another device configuration that was explored in this study was a Quantum Point Contact (QPC) on Bernal bilayer graphene. The device was made by picking up a pre-patterned top graphite gate on hBN, and used to make a device with bilayer graphene as the channel material. The aim was to be able to electrostatically gate Bilayer graphene differently in four isolated regions of the device, to create a QPC by tuning to wide regions of the channel to a resistive state, forming a narrow constriction only allows quantized channels of conductance. The image of the device (Fig. 12c). While we were able to successfully isolate the four quadrants of the top gate (labelled North(N), South(S), East(E), and West(W))[8], we were not able to observe QPC behaviour in the device. This is because the electrode connecting to the bottom gate was physically disconnected, due to an error in the device design. This meant that we were not able to apply any bias to the bottom gate, limiting our ability to tune the potential in the constriction.

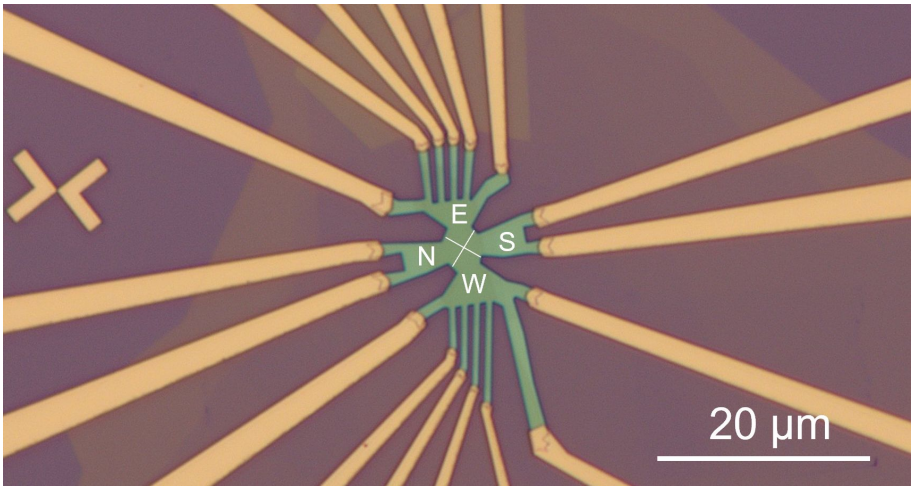

Figure 30: Image of the QPC device with the top gate quadrants labelled N, S, E, W

We were however able to apply up to 10V of DC bias on each of the quadrants of the top gate and measure the leakage current with all other electrodes grounded. This means we were able to apply 10V of DC bias across the narrow constriction of 64 nm, showing the robustness of this device architecture.

Chapter 4

Conclusion and Outlook

4.1 Conclusion

In this study, we explored the fabrication and characterization of graphene heterostructures, particularly twisted monolayer-bilayer graphene (tMBG) devices. We tried to understand how rotational misalignment influences electronic transport properties. The study involved optimising the fabrication techniques, conducting low temperature transport measurements, and exploring nanoscale imaging methods.

The fabrication of high-quality graphene devices require precise control over material transfer and device design. We used mechanical exfoliation of van der Waals materials, and dry transfer techniques to assembled heterostructures of graphene. The transfer of materials was performed at an elevated temperature to improve the homogeneity of the structures. We also used AFM lithography for precise patterning of different layers before assembly. Standard fabrication techniques were employed to process the stack of 2D materials into a

functional device.

We successfully fabricated and characterized several tMBG devices, and noted the variability in the twist angle of the devices. We demonstrated that the band structure of graphene can be tuned[15] via rotational alignment and electrostatic gating, leading to distinct insulating phases at certain filling factors, due to the emergence of flat bands[15]. We also observed van Hove singularities that can be tuned by displacement field, indicating a strongly tunable band structure. In addition, we explored the imaging of moiré superlattices using Lateral Force Microscopy (LFM), and were able to indirectly observe the moiré pattern in twisted bilayer graphene. Finally, we designed and fabricated a Quantum Point Contact(QPC) on Bernal bilayer graphene, which was able to withstand high DC bias across a narrow constriction (64 nm) without breakdown. Further modification of the device design can help fully realise its intended functionality.

4.2 Outlook

The results in this work add to the understanding of correlated electronic phases in moiré superlattices. The observation of correlated insulating states at half-filling[15] aligns with previous findings in tBLG[25] and tMBG[29], further supporting the universality of interaction-driven phases in moiré materials. This platform has been used to achieve electric switching of orbital ferromagnetic states[29], which has applications in embedded magnetic memory in logic devices. The coexistence of superconductivity and non-trivial Chern insulating states in superconducting moiré systems[25] can pave the way for topological qubits[18] that are robust against local perturbations. The similarity between the family of high T_c cuprate superconductors and moiré superconducting systems indicates that tunability of these systems can be used to understand the superconducting pairing mechanisms that can help construct new systems with enhanced superconductivity including room temperature superconductivity[26].

Beyond moiré graphene, there is growing interested in investigating flatband superconductivity and correlated states in ABC (rhombohedral) stacked graphene. They do not necessarily rely on a moiré superlattice to generate flat bands and have become an attractive platform to realise exotic phenomenon like Fractional Quantum Anomalous Hall Effect (FQAHE), chiral superconductivity and Chern insulators.

Our application of Lateral Force Microscopy (LFM) for detecting moiré patterns in ambient conditions offers a promising avenue for twist angle screening and studying local

twist angle disorder. This can be useful in understanding the contribution of twist angle disorder to the transport properties of moiré devices.

The use of split-gate geometries to create Quantum Point Contact (QPC) like constrictions in graphene devices offers a versatile way to explore edge-state interference and other mesoscopic phenomena[8] [9]. In particular, controlling individual edge channels in the quantum Hall regime allows one to probe the quantum interference of chiral edge states - analogous to Fabry-Pérot interferometer geometry for electrons - and investigate fractional quasiparticles, Berry phases, and potential anyonic statistics in more excited fractional quantum Hall states[31] [19].

In summary, studying unusual stacking orders in graphene illustrate how rich correlated physics can arise in 2D sheets of carbon atoms. The flexibility of working with graphene also allows the design of novel device architectures that can shed light on new physics and translate into useful applications.

Bibliography

[1] M. Aliofkhazraei, N. Ali, W. I. Milne, C. S. Ozkan, S. Mitura, and J. L. Gervasoni, editors. *Graphene Science Handbook: Electrical and Optical Properties*. CRC Press, 1st edition, 2016. doi: 10.1201/b19642. URL https://doi.org/10.1201/b19642.

[2] Liheng An. *Device Fabrication and Quantum Transport Characterization of Atomically Thin Two-Dimensional Materials*. PhD thesis, 2020. URL https://www.proquest.com/dissertations-theses/device-fabrication-quantum-transport/docview/3132860721/se-2. Copyright - Database copyright ProQuest LLC; ProQuest does not claim copyright in the individual underlying works; Last updated - 2024-11-26.

[3] Saisab Bhowmik, Arindam Ghosh, and U Chandni. Emergent phases in graphene flat bands. *Reports on Progress in Physics*, 87(9):096401, aug 2024. doi: 10.1088/1361-6633/ad67ed. URL https://dx.doi.org/10.1088/1361-6633/ad67ed.

[4] Rafi Bistritzer and Allan H. MacDonald. Moiré bands in twisted double-layer graphene. *Proceedings of the National Academy of Sciences*, 108(30):12233–12237, 2011. doi: 10.1073/pnas.1108174108. URL https://www.pnas.org/doi/abs/10.1073/pnas.1108174108.

[5] Yuan Cao, Valla Fatemi, Ahmet Demir, Shiang Fang, Spencer L. Tomarken, Jason Y. Luo, Javier D. Sanchez-Yamagishi, Kenji Watanabe, Takashi Taniguchi, Efthimios Kaxiras, Ray C. Ashoori, and Pablo Jarillo-Herrero. Correlated insulator behaviour at half-filling in magic-angle graphene superlattices. *Nature*, 556(7699):80–84, Apr 2018. ISSN 1476-4687. doi: 10.1038/nature26154. URL https://doi.org/10.1038/nature26154.

[6] Yuan Cao, Valla Fatemi, Shiang Fang, Kenji Watanabe, Takashi Taniguchi, Efthimios Kaxiras, and Pablo Jarillo-Herrero. Unconventional superconductivity in magic-angle graphene superlattices. *Nature*, 556(7699):43–50, Apr 2018. ISSN 1476-4687. doi: 10.1038/nature26160. URL https://doi.org/10.1038/nature26160.

[7] Shaowen Chen, Minhao He, Ya-Hui Zhang, Valerie Hsieh, Zaiyao Fei, K. Watanabe, T. Taniguchi, David H. Cobden, Xiaodong Xu, Cory R. Dean, and Matthew Yankowitz. Electrically tunable correlated and topological states in twisted monolayer–bilayer graphene. *Nature Physics*, 17(3):374–380, Mar 2021. ISSN 1745-2481. doi: 10.1038/s41567-020-01062-6. URL https://doi.org/10.1038/s41567-020-01062-6.

[8] Liam A. Cohen, Noah L. Samuelson, Taige Wang, Kai Klocke, Cian C. Reeves, Takashi Taniguchi, Kenji Watanabe, Sagar Vijay, Michael P. Zaletel, and Andrea F. Young. Nanoscale electrostatic control in ultraclean van der Waals heterostructures by local anodic oxidation of graphite gates. *Nature Physics*, 19(10):1502–1508, October 2023. ISSN 1745-2481. doi: 10.1038/s41567-023-02114-3. URL https://www.nature.com/articles/s41567-023-02114-3. Publisher: Nature Publishing Group.

[9] Liam A. Cohen, Noah L. Samuelson, Taige Wang, Kai Klocke, Cian C. Reeves, Takashi Taniguchi, Kenji Watanabe, Sagar Vijay, Michael P. Zaletel, and Andrea F. Young. Spontaneous localization at a potential saddle point from edge state reconstruction in a quantum hall point contact. *Phys. Rev. Lett.*, 134:076302, Feb 2025. doi: 10.1103/PhysRevLett.134.076302. URL https://link.aps.org/doi/10.1103/PhysRevLett.134.076302.

[10] C. R. Dean, A. F. Young, I. Meric, C. Lee, L. Wang, S. Sorgenfrei, K. Watanabe, T. Taniguchi, P. Kim, K. L. Shepard, and J. Hone. Boron nitride substrates for high-quality graphene electronics. *Nature Nanotechnology*, 5(10):722–726, Oct 2010. ISSN 1748-3395. doi: 10.1038/nnano.2010.172. URL https://doi.org/10.1038/nnano.2010.172.

[11] Alain Diebold and Tino Hofmann. *Optical and Electrical Properties of Nanoscale Materials*. 01 2021. ISBN 978-3-030-80322-3. doi: 10.1007/978-3-030-80323-0.

[12] J. Diez-Merida, I. Das, G. Di Battista, A. Diez-Carlon, M. Lee, L. Zeng, K. Watanabe, T. Taniguchi, E. Olsson, and D. K. Efetov. High-yield fabrication of bubble-free magic-angle twisted bilayer graphene devices with high twist-angle homogeneity, 2024. URL https://arxiv.org/abs/2405.11323.

[13] Jaime Díez-Mérida, Ipsita Das, Giorgio Di Battista, Andrés Díez-Carlón, Martin Lee, Lunjie Zeng, Kenji Watanabe, Takashi Taniguchi, Eva Olsson, and Dmitri K. Efetov. High-yield fabrication of bubble-free magic-angle twisted bilayer graphene devices with high twist-angle homogeneity. *Newton*, 1(1), Mar 2025. ISSN 2950-6360. doi: 10.1016/j.newton.2024.100007. URL https://doi.org/10.1016/j.newton.2024.100007.

[14] Steven M. Girvin and Kun Yang. *Modern Condensed Matter Physics*. Cambridge University Press, 2019.

[15] Minhao He, Ya-Hui Zhang, Yuhao Li, Zaiyao Fei, Kenji Watanabe, Takashi Taniguchi, Xiaodong Xu, and Matthew Yankowitz. Competing correlated states and abundant orbital magnetism in twisted monolayer-bilayer graphene. *Nature Communications*, 12 (1):4727, Aug 2021. ISSN 2041-1723. doi: 10.1038/s41467-021-25044-1. URL https://doi.org/10.1038/s41467-021-25044-1.

[16] Yuan Huang, Eli Sutter, Norman N. Shi, Jiabao Zheng, Tianzhong Yang, Dirk Englund, Hong-Jun Gao, and Peter Sutter. Reliable exfoliation of large-area high-quality flakes of graphene and other two-dimensional materials. *ACS Nano*, 9(11):10612–10620, Nov 2015. ISSN 1936-0851. doi: 10.1021/acsnano.5b04258. URL https://doi.org/10.1021/acsnano.5b04258.

[17] Maëlle Kapfer, Bjarke S. Jessen, Megan E. Eisele, Matthew Fu, Dorte R. Danielsen, Thomas P. Darlington, Samuel L. Moore, Nathan R. Finney, Ariane Marchese, Valerie Hsieh, Paulina Majchrzak, Zhihao Jiang, Deepnarayan Biswas, Pavel Dudin, José Avila, Kenji Watanabe, Takashi Taniguchi, Søren Ulstrup, Peter Bøggild, P. J. Schuck, Dmitri N. Basov, James Hone, and Cory R. Dean. Programming twist angle and strain profiles in 2d materials. *Science*, 381(6658):677–681, 2023. doi: 10.1126/science.ade9995. URL https://www.science.org/doi/abs/10.1126/science.ade9995.

[18] Maryam Khosravian, Elena Bascones, and Jose L Lado. Moiré-enabled topological superconductivity in twisted bilayer graphene. *2D Materials*, 11(3):035012, apr 2024. doi: 10.1088/2053-1583/ad3b0c. URL https://dx.doi.org/10.1088/2053-1583/ad3b0c.

[19] Jehyun Kim, Himanshu Dev, Ravi Kumar, Alexey Ilin, André Haug, Vishal Bhardwaj, Changki Hong, Kenji Watanabe, Takashi Taniguchi, Ady Stern, and Yuval Ronen.

Aharonov–bohm interference and statistical phase-jump evolution in fractional quantum hall states in bilayer graphene. *Nature Nanotechnology*, 19(11):1619–1626, Nov 2024. ISSN 1748-3395. doi: 10.1038/s41565-024-01751-w. URL https://doi.org/10.1038/s41565-024-01751-w.

[20] Kyounghwan Kim, Matthew Yankowitz, Babak Fallahazad, Sangwoo Kang, Hema C. P. Movva, Shengqiang Huang, Stefano Larentis, Chris M. Corbet, Takashi Taniguchi, Kenji Watanabe, Sanjay K. Banerjee, Brian J. LeRoy, and Emanuel Tutuc. van der waals heterostructures with high accuracy rotational alignment. *Nano Letters*, 16(3):1989–1995, Mar 2016. ISSN 1530-6984. doi: 10.1021/acs.nanolett.5b05263. URL https://doi.org/10.1021/acs.nanolett.5b05263.

[21] Mahito Kohmoto. Topological invariant and the quantization of the hall conductance. *Annals of Physics*, 160(2):343–354, 1985. ISSN 0003-4916. doi: https://doi.org/10.1016/0003-4916(85)90148-4. URL https://www.sciencedirect.com/science/article/pii/0003491685901484.

[22] Guohong Li, A. Luican, J. M. B. Lopes dos Santos, A. H. Castro Neto, A. Reina, J. Kong, and E. Y. Andrei. Observation of van hove singularities in twisted graphene layers. *Nature Physics*, 6(2):109–113, Feb 2010. ISSN 1745-2481. doi: 10.1038/nphys1463. URL https://doi.org/10.1038/nphys1463.

[23] Guohong Li, A. Luican, J. M. B. Lopes dos Santos, A. H. Castro Neto, A. Reina, J. Kong, and E. Y. Andrei. Observation of van hove singularities in twisted graphene layers. *Nature Physics*, 6(2):109–113, Feb 2010. ISSN 1745-2481. doi: 10.1038/nphys1463. URL https://doi.org/10.1038/nphys1463.

[24] Hongyuan Li, Zhe Ying, Bosai Lyu, Aolin Deng, Lele Wang, Takashi Taniguchi, Kenji Watanabe, and Zhiwen Shi. Electrode-free anodic oxidation nanolithography of low-dimensional materials. *Nano Letters*, 18(12):8011–8015, Dec 2018. ISSN 1530-6984. doi: 10.1021/acs.nanolett.8b04166. URL https://doi.org/10.1021/acs.nanolett.8b04166.

[25] Xiaobo Lu, Petr Stepanov, Wei Yang, Ming Xie, Mohammed Ali Aamir, Ipsita Das, Carles Urgell, Kenji Watanabe, Takashi Taniguchi, Guangyu Zhang, Adrian Bachtold, Allan H. MacDonald, and Dmitri K. Efetov. Superconductors, orbital magnets and correlated states in magic-angle bilayer graphene. *Nature*, 574(7780):653–657, Oct 2019. ISSN 1476-4687. doi: 10.1038/s41586-019-1695-0. URL https://doi.org/10.1038/s41586-019-1695-0.

[26] Ivar Martin. Moiré superconductivity. *Annals of Physics*, 417:168118, 2020. ISSN 0003-4916. doi: https://doi.org/10.1016/j.aop.2020.168118. URL https://www.sciencedirect.com/science/article/pii/S0003491620300518. Eliashberg theory at 60: Strong-coupling superconductivity and beyond.

[27] David Nečas and Petr Klapetek. Gwyddion: Open-source software for spm data analysis. https://gwyddion.net/, 2025. Version 2.67.

[28] K. S. Novoselov, A. K. Geim, S. V. Morozov, D. Jiang, Y. Zhang, S. V. Dubonos, I. V. Grigorieva, and A. A. Firsov. Electric field effect in atomically thin carbon films. *Science*, 306(5696):666–669, 2004. doi: 10.1126/science.1102896. URL https://www.science.org/doi/abs/10.1126/science.1102896.

[29] H. Polshyn, J. Zhu, M. A. Kumar, Y. Zhang, F. Yang, C. L. Tschirhart, M. Serlin, K. Watanabe, T. Taniguchi, A. H. MacDonald, and A. F. Young. Electrical switching of magnetic order in an orbital chern insulator. *Nature*, 588(7836):66–70, Dec 2020. ISSN 1476-4687. doi: 10.1038/s41586-020-2963-8. URL https://doi.org/10.1038/s41586-020-2963-8.

[30] Louk Rademaker, Ivan V. Protopopov, and Dmitry A. Abanin. Topological flat bands and correlated states in twisted monolayer-bilayer graphene. *Phys. Rev. Res.*, 2:033150, Jul 2020. doi: 10.1103/PhysRevResearch.2.033150. URL https://link.aps.org/doi/10.1103/PhysRevResearch.2.033150.

[31] Noah L. Samuelson, Liam A. Cohen, Will Wang, Simon Blanch, Takashi Taniguchi, Kenji Watanabe, Michael P. Zaletel, and Andrea F. Young. Anyonic statistics and slow quasiparticle dynamics in a graphene fractional quantum hall interferometer, 2024. URL https://arxiv.org/abs/2403.19628.

[32] M. Serlin, C. L. Tschirhart, H. Polshyn, Y. Zhang, J. Zhu, K. Watanabe, T. Taniguchi, L. Balents, and A. F. Young. Intrinsic quantized anomalous hall effect in a moiré heterostructure. *Science*, 367(6480):900–903, 2020. doi: 10.1126/science.aay5533. URL https://www.science.org/doi/abs/10.1126/science.aay5533.

[33] Aaron L. Sharpe, Eli J. Fox, Arthur W. Barnard, Joe Finney, Kenji Watanabe, Takashi Taniguchi, M. A. Kastner, and David Goldhaber-Gordon. Emergent ferromagnetism near three-quarters filling in twisted bilayer graphene. *Science*, 365(6453):605–608, 2019. doi: 10.1126/science.aaw3780. URL https://www.science.org/doi/abs/10.1126/science.aaw3780.

[34] D. J. Thouless, M. Kohmoto, M. P. Nightingale, and M. den Nijs. Quantized hall conductance in a two-dimensional periodic potential. *Phys. Rev. Lett.*, 49:405–408, Aug 1982. doi: 10.1103/PhysRevLett.49.405. URL https://link.aps.org/doi/10.1103/PhysRevLett.49.405.

[35] David Tong. Lectures on the quantum hall effect, 2016. URL https://arxiv.org/abs/1606.06687.

[36] Charles L. Tschirhart. *Berry Curvature, Orbital Magnetism, and Chern Magnets in van der Waals Heterostructures*. PhD thesis, 2023. URL https://www.proquest.com/dissertations-theses/berry-curvature-orbital-magnetism-chern-magnets/docview/2811129099/se-2. Copyright - Database copyright ProQuest LLC; ProQuest does not claim copyright in the individual underlying works; Last updated - 2023-05-11.

[37] Léon Van Hove. The occurrence of singularities in the elastic frequency distribution of a crystal. *Phys. Rev.*, 89:1189–1193, Mar 1953. doi: 10.1103/PhysRev.89.1189. URL https://link.aps.org/doi/10.1103/PhysRev.89.1189.

[38] L. Wang, I. Meric, P. Y. Huang, Q. Gao, Y. Gao, H. Tran, T. Taniguchi, K. Watanabe, L. M. Campos, D. A. Muller, J. Guo, P. Kim, J. Hone, K. L. Shepard, and C. R. Dean. One-dimensional electrical contact to a two-dimensional material. *Science*, 342(6158): 614–617, 2013. doi: 10.1126/science.1244358. URL https://www.science.org/doi/abs/10.1126/science.1244358.

[39] Shuigang Xu, Mohammed M. Al Ezzi, Nilanthy Balakrishnan, Aitor Garcia-Ruiz, Bonnie Tsim, Ciaran Mullan, Julien Barrier, Na Xin, Benjamin A. Piot, Takashi Taniguchi, Kenji Watanabe, Alexandra Carvalho, Artem Mishchenko, A. K. Geim, Vladimir I. Fal'ko, Shaffique Adam, Antonio Helio Castro Neto, Kostya S. Novoselov, and Yanmeng Shi. Tunable van hove singularities and correlated states in twisted monolayer–bilayer graphene. *Nature Physics*, 17(5):619–626, May 2021. ISSN 1745-2481. doi: 10.1038/s41567-021-01172-9. URL https://doi.org/10.1038/s41567-021-01172-9.

[40] Yuanbo Zhang, Tsung-Ta Tang, Caglar Girit, Zhao Hao, Michael C. Martin, Alex Zettl, Michael F. Crommie, Y. Ron Shen, and Feng Wang. Direct observation of a widely tunable bandgap in bilayer graphene. *Nature*, 459(7248):820–823, Jun 2009. ISSN 1476-4687. doi: 10.1038/nature08105. URL https://doi.org/10.1038/nature08105.